Investigation of Photoproduced Events from the H1 Detector at HERA

Edward Hanlon B.Sc.

University Of Lancaster

Dec 1993

This thesis is submitted in partial fulfilment of the degree of Ph.D. at the University of Lancaster. No part of it has been, or will be, submitted to any other University.

Acknowledgements

I would like to thank my supervisor, Arthur Clegg, for giving me the opportunity to study at Lancaster, for giving me the benefit of his experience and for his continued support, involvement and genuine interest in my studies. Thanks to Rob and Alex for their diligent maintainance of the Lancaster Vax cluster and their cheerful countenance in their daily battle with the bugs. Thanks to Steve for not castigating me when I occasionally poured my coffee into the computers. Special thanks to Stephen Burke for setting up the H1 software for VAX and thus making this thesis possible. Thanks to Camille for that lovely flat in Stellingen. Thanks to the Lancaster Lads: Dug, Dave, Ed, Jeff, Mike and Mark for demonstrating the universality of experience. Thanks to all those at DESY for the coffee breaks , Saturday night excursions and Friday nights at the F&F. Thanks to Ian Walker just for being there (wherever that was!). Thanks to Angie and Micky, Soheila, Ulriche and Meite for making me feel at home in Hamburg. Thanks to the rest of my friends and finally thanks to my family for their support.

I acknowledge that the funding for this research was provided by SERC.

Dedicated to my mother

"I know no-o-othing." *Manuel, Flawtey Towers*

Abstract

Using data collected by the H1 Collaboration between August and October 1992 an almost background free sample of 611 photon-proton events with tagged electron and drift chamber triggers has been collected. This corresponds to a cross section in electron proton collision of

$$\sigma = 28 \pm 1_{\mathrm{stat}}{}^{+17}_{-11\,\mathrm{syst}} \text{ nb.}$$

This has been compared to full Monte Carlo simulation using PYTHIA version 5.6 to generate 'hard' QCD 2 body scattering with proton and photon structure functions MRSD0 and LAC2 or MRSD- and LAC1a. The former combination suggests a value of 2 and the latter at least 3GeV/c for the cutoff parameter P_T^{min} to achieve consistency with the cross section measured.

Studies of the inclusive distributions of tracks and the clustering of energy deposits show general agreement with the above simulation suggesting little contamination from low transverse momentum transfer processes.

Contents

List of Figures

List of Tables

Chapter 1

The Theory of Photon-Proton Interactions

This chapter aims to review the theory of hadron production in photon-proton interactions, with emphasis on practical implementation. In order to introduce the idea of structure functions and associated variables I first concentrate on Deep Inelastic Scattering (DIS). At the end I discuss some points concerning showering and fragmentation before giving details of computer simulation of the physics processes.

1.1 Structure Functions

1.1.1 An Introduction to Variables

The basic process under consideration is the scattering of electrons from protons as depicted in Figure 1.1. An incoming electron, described by the 4-momentum k, emits a virtual photon, q, and is thus deflected with altered kinematics, k', leading to the relation

$$q = k - k'. \tag{1.1}$$

This virtual photon is absorbed by the incoming proton, P, of mass M, which leads to a hadronic final state, P', of invariant mass W. I may also introduce ν and θ, the energy lost by the electron and its angle of deflection in the proton rest

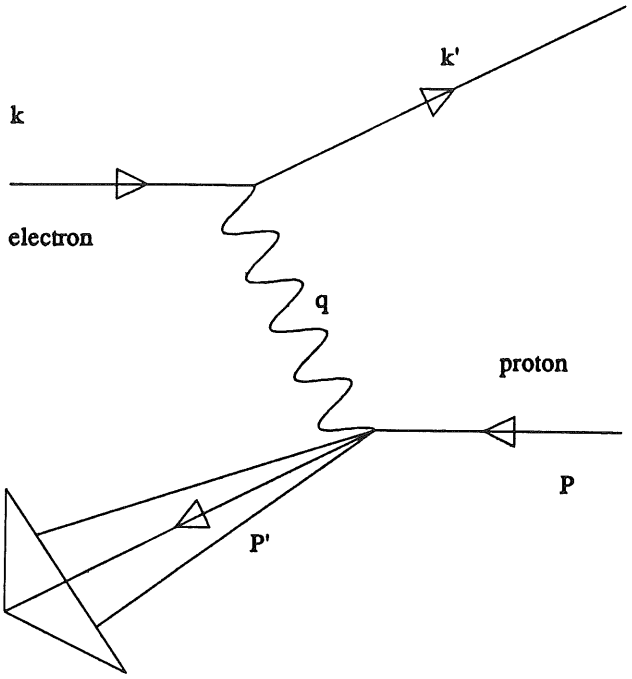

Figure 1.1: Kinematical variables of electron-proton scattering

frame. Also, for convenience, I shall define Q^2, a positive quantity which is minus the invariant mass squared of the exchanged photon. It is worth noting that,

$$P.q = M\nu \tag{1.2}$$

and

$$W^2 = M^2 + 2M\nu - Q^2. \tag{1.3}$$

It will also be useful to introduce a variable ξ, the fraction of proton momentum carried by an interacting subunit of mass, m. Elastic scattering of this subunit leads to the condition

$$(\xi P + q)^2 = m^2 \tag{1.4}$$

and hence

$$\xi = \frac{Q^2 + m^2}{M\left(\nu + \sqrt{\nu^2 + Q^2 + m^2}\right)} \tag{1.5}$$

which in the limit of $\nu^2 \gg Q^2 \gg m^2$ becomes

$$\xi = \frac{Q^2}{2M\nu} \equiv x \tag{1.6}$$

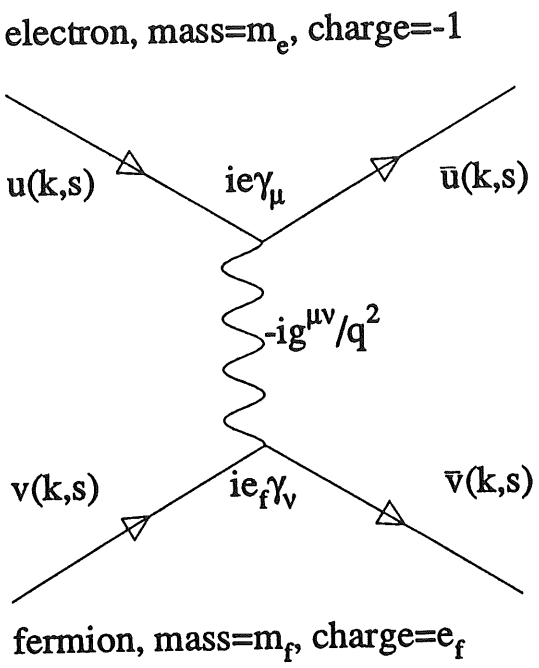

Figure 1.2: Feynman Diagram for general elastic electron-fermion scattering

thus defining Bjorken-x, x.

Another variable often used in this domain is y defined by

$$y = \frac{P.q}{P.k} \tag{1.7}$$

1.1.2 The Scattering of Electrons from Fermions

I will assume throughout the following that the reader is acquainted with the basic principles and techniques of perturbative QED as widely covered in student texts [1]. I shall avoid any details of the techniques in order that the flow of argument remains uninterrupted. The Feynman Diagram describing the first order elastic scattering of an electron from another pointlike fermion of charge e_f and mass m_f is shown in Figure 1.2. From this we may use the Feynman rules to write down the particular combination of spinors, vertex matrices and propagators which when squared, summed over final spin states, averaged over initial spin states and combined with the appropriate phase space factors reveal the correct differential cross section.

$$\frac{d\sigma}{d\Omega} = \left(\frac{\alpha^2}{4k^2\sin^4(\theta/2)}\cos^2(\theta/2)\frac{k'}{k}\right)e_f^2\left(1-\frac{q^2\tan^2(\theta/2)}{2m_f^2}\right) \tag{1.8}$$

We may rearrange this equation to write it as a differential of the variables described earlier,

$$\frac{d^2\sigma}{dQ^2 d\nu} = \frac{\pi\alpha^2}{4k^2\sin^4(\theta/2)}\frac{1}{kk'}\left[\cos^2(\theta/2) + \left(\frac{Q^2}{2M^2}\right)\sin^2(\theta/2)\right]\delta\left(\nu - \frac{Q^2}{2M}\right) \tag{1.9}$$

Notice the two terms in the square brackets. The first describes the interaction of charges whilst the second describes the interaction of magnetic moments. Notice also the delta function which is required in elastic interactions where Q^2 and ν are not independent.

The proton is also a charged object with half integer spin although it has extended charge distribution and may interact inelastically. Nevertheless its differential cross section may be similarly derived if these aspects are taken into consideration and the restrictions of Lorentz Invariance and current conservation are applied. Thus we obtain

$$\frac{d^2\sigma}{dQ^2 d\nu} = \frac{\pi\alpha^2}{4k^2\sin^4(\theta/2)}\frac{1}{kk'}\left[W_2\left(Q^2,\nu\right)\cos^2(\theta/2) + 2W_1\left(Q^2,\nu\right)\sin^2(\theta/2)\right] \tag{1.10}$$

The delta-function has now disappeared, reflecting the independence of Q^2 and ν in inelastic scattering. Here W_1 and W_2 are form factors introduced to parameterize the unknown details about the distribution of charge and magnetic moment in the proton. This does not seem to be particularly useful, as without a theory of the constituents of the proton we can only measure these form factors and have no predictions with which we may make comparisons. Luckily the parton model comes to our rescue (although in reality it was the measurements of W_1 and W_2 which confirmed magnificently the parton model). In this theory the proton constituents are quarks which, at the energy scale of Deep Inelastic Scattering (DIS), can be considered as freely moving. In accordance with the Heisenberg Uncertainty Principle, at large energy transfer scales the virtual exchange photon probes a very small area for a very short time. If in this limit the partons are unlikely to interact with each other they may be considered essentially free. The quarks are charged fermions which are supposed to interact "quasi-elastically" and therefore their scattering must be described by equation 1.9. Simple comparison

between this equation and that of the proton yields the contribution to the form factors from a quark i as,

$$W_1^i = e_i^2 \frac{Q^2}{4M^2x^2}\delta\left(\nu - \frac{Q^2}{2Mx}\right) \tag{1.11}$$

$$W_2^i = e_i^2 \delta\left(\nu - \frac{Q^2}{2Mx}\right) \tag{1.12}$$

where x denotes the fraction of proton momentum carried by the quark. In order to return the full form factor we must sum over all the different types of parton and integrate across the spectrum of x using the parton density function $f_i(x)$, which describes the probability of finding a parton of type i with momentum fraction x.

$$W_2\left(\nu, Q^2\right) = \sum_i \int_0^1 dx f_i(x) e_i^2 \delta\left(\nu - \frac{Q^2}{2Mx}\right). \tag{1.13}$$

Using the relationship

$$\delta\left(\nu - \frac{Q^2}{2Mx}\right). = \left(\frac{x}{\nu}\right)\delta\left(x - \frac{Q^2}{2M\nu}\right). \tag{1.14}$$

we finally reach

$$\nu W_2\left(\nu, Q^2\right) = \sum_i e_i^2 x f_i(x) \equiv F_2(x) \tag{1.15}$$

and similarly

$$MW_1\left(\nu, Q^2\right) = F_1(x) \tag{1.16}$$

F_1 and F_2 are called structure functions and display the neat property that they no longer depend on the two variables ν and Q^2 but rather on their ratio ($x = Q^2/2M\nu$). This property is known as scaling and is derived from the "quasi-elastic" scattering of the partons, just as the elastic pointlike cross section formula required a delta function to fix the relationship.

Furthermore, the structure functions may be considered the incoherent sum of quark distributions in the proton weighted by the square of the quarks charge, e.g.

$$F_2^p = x\{(4/9)[u(x) + \overline{u}(x)] + (1/9)[d(x) + \overline{d}(x) + s(x) + \overline{s}(x)]...\} \tag{1.17}$$

These quark distributions must satisfy certain conditions such as providing an integrated charge of 1 unit. The u and d structure functions of the proton are

related by isospin inversion to those of the neutron. By comparing proton and neutron interactions with electrons and neutrinos these separate distributions can be dug out of the data.

It is the ability to resolve a hadron into its constituent partons that allows one to generalize and make predictions about interactions other than DIS. For example, colliding proton beams can, when the momentum transfer occurring is high enough, be considered as beams of free partons of different types with momentum distributions as described by the parton density functions. As the reaction of parton-parton annihilation to electron-positron pairs is calculable in QED, it is possible, given the parton flux, to predict the rate and distribution of their production. Unfortunately DIS cannot measure the structure function of the uncharged gluons and hence this must be inferred from less direct techniques, such as the momentum sum rule constraint or scaling violations of the quark distributions.

1.1.3 Scaling Violations and the Altarelli-Parisi Equations

In reality the structure functions do not scale perfectly with x, which reflects the fact that the partons are not entirely free. QCD predicts that quarks may radiate a gluon thus splitting their energy between 2 partons. At a low Q^2 the photon will have low resolution and hence cannot distinguish the quark-gluon system from a single quark. As Q^2 increases so the virtual exchanged photon is able to resolve smaller scales and thus pick out the quark separately. Thus the tendency with rising Q^2 is for the partons to lose momentum but gain in number or, put another way, rising Q^2 causes a reduction in the structure functions at high x with a corresponding increase at low x. Luckily it is possible to predict this change using QCD. The variation only occurs with the logarithm of Q^2 and is described by the Altarelli-Parisi Equations [2];

$$\frac{df(x,\ln Q^2)}{d\ln Q^2} = \frac{\alpha_s(Q^2)}{2\pi}\int_x^1 \frac{dy}{y} f(y,\ln Q^2) P_{qq}\left(\frac{x}{y}\right) \qquad (1.18)$$

$P_{ab}(z)$ is called a splitting function and defines the probability that parton a will split from parton b carrying with it a fraction $z(=x/y)$ of b's momentum. In the case of quarks splitting from quarks this is given by

$$P_{qq}(z) = \frac{4}{3}\left(\frac{1+z^2}{1-z}\right) \tag{1.19}$$

In addition to quarks splitting into a gluon and quark, gluons may split into a pair of gluons or a quark-antiquark pair. In this way the various parton density functions evolve into each other.

Since the data presently existing has been limited by the energy ranges available, the low-x region remains unmeasured. All predictions in this domain are extrapolations and hence wide variations occur. Once the parton density is high enough, there are bound to be interactions between them modifying the evolution. Low-x physics will be a major research area at HERA [3].

It has been suggested that events with more than one parton-parton collision may exist leading to eikonalized structure functions. Recent studies have shown that analysis of event shapes may shed light on this subject, but would require greater luminosity than is presently available [4, 5].

1.2 An Overview of Photoproduction Models

Most interactions at HERA involve photons radiated from electrons with little or no deflection. These have very low Q^2 value and hence are considered 'nearly on-shell'. The subsequent gamma-proton events are called photoproduction. The interactions are governed by the laws of QCD via the photon coupling to quark anti-quark pairs. In practice QCD cannot predict all the possible interactions as many are in regimes where perturbative-QCD is inapplicable. In order to obtain a complete picture of possible interactions three distinct models must be combined. Although these allow insights into the likely nature of photoproduction events, they are unable to provide precise predictions. Instead measured photon structure functions from photon-photon studies must be used for detailed comparisons. Many interrelated processes and parameters are involved including: the low Q^2 limit of hard scattering; errors arising from incoherent addition of subprocesses; approximation to leading order QCD; the relative contributions of the three models; the structure functions used; the QCD radiative showering; and the

fragmentation scheme. Data from many experiments and theoretical insight must be combined to impose sensible constraints.

1.3 Classifying Photon-Proton Collisions

It is useful to subdivide the possible interaction processes in terms of possible configurations of the incoming particle on the photon side. As depicted in Figures 1.3, 1.4 and 1.5 events can fall into one of the following categories.

- Direct
  - ◇ The photon itself takes part in the hard interaction being directly absorbed by a parton in the proton.
- Vector Dominance Model (VDM)
  - ◇ The photon couples to quark-antiquark pairs which are produced with low mutual transverse momenta and hence low virtualities. This state survives long enough for the quarks to interact and form a vector meson state. Thereafter the scenario is directly equivalent to meson-proton collision.
- Quark Parton Model (QPM)
  - ◇ The photon couples to quark-antiquark pairs which are produced with high enough mutual transverse momenta to be treated by perturbative QCD. After evolution through emission of gluons one of these virtual partons may scatter from a parton in the proton.

In these processes there is no scattered electron available to define the virtuality scale and so the square of transverse momenta must be used.

At the lowest scales, below the valid region of perturbative QCD, the only contributing processes arise from the VDM interpretation. At a higher virtuality scale the cross section for hard QCD resolved and direct perturbative processes becomes dominant. In first order these are simply 2 body scattering events as

shown in Figure 1.2. A detailed anthology of Feynman-diagrams and the resulting matrix elements is given in Appendix A.

The $\mathcal{O}(\alpha_s^2)$ parton-parton interaction of resolved contributions is convoluted with the initial $\mathcal{O}(\alpha/\alpha_s)$ process of photon splitting rendering this channel of comparable likelihood to the $\mathcal{O}(\alpha\alpha_s)$ direct photon-parton interaction .

The most important parameter of these processes is the minimum transverse momentum at which scattering is allowed, P_T^{min}. It forms the lower limit of integration in cross section calculation. The overall cross-section is very sensitive to this parameter as the distribution rises rapidly with decreasing P_T. Studies of photon-photon collision from the AMY [7] and TOPAZ [8] collaborations at KEK have suggested values of 1.4 and 1.6GeV/c respectively, whereas a recent study of photon-photon collisions from ALEPII [9] at LEP required a much larger value of 2.5GeV/c. First results from the HERA collaborations, H1 [10] and ZEUS [11], favour a P_T^{MIN} above 2.0GeV/c to fit the overall photon-proton cross section.

1.3.1 Direct Processes

In direct processes the photon interacts directly with partons inside the proton. QCD Compton Scattering Fig A.9 and Photon-Gluon Fusion Fig A.10 are the contributing subprocesses. These are calculable from QCD theory using proton structure functions but require the parameter P_T^{min} to determine the threshold at which the processes turn on.

The Photon-Gluon Fusion processes are of particular interest due to the possibility of charm production. Charm identification allows a sample of high purity to be obtained from these events and the absence of photon structure function makes them ideal for investigating the gluon structure functions of the proton.

These events have a final state comprising, in the lowest order, the two scattered parton jets and a third jet from the leftover proton fragments which continue into the forward part of the detector. This could be distinguishable from the resolved case (discussed in section 1.4) where some photon fragments remain and might be detectable in the rear part of the detector. Unfortunately the resolved processes outnumber the direct processes by about 10 to 1 in this low Q^2 region hampering

Figure 1.3: Direct Interaction

Figure 1.4: Vector Dominance Model

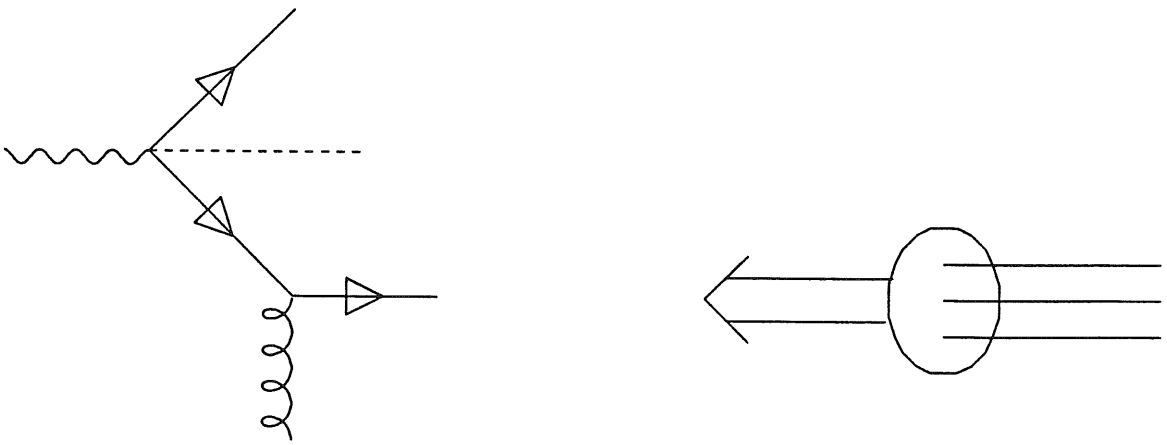

Figure 1.5: Quark Parton Model

attempts to produce a purified sample of direct events. Furthermore the backward region of the calorimeter is the least well instrumented and it is possible for particles to escape detection completely by remaining within the beam pipe.

1.3.2 The Vector Dominance Model (VDM)

This model grew from observations at fixed target experiments where gamma-nucleon collisions produced similar final states to pion-nucleon collision [12, 13]. It is assumed that a photon may fluctuate temporarily into a hadronic state preserving the discrete quantum numbers $J^{PC}\,(1^{--})$ thus forming a vector meson such as a ρ, ω or ϕ. Subsequent interactions are treated as meson-proton collisions.

At low momentum transfers there are elastic and diffractive scattering events in which the incoming meson and proton interact to form a final state containing a meson and a baryon. These events may also lead to disintegration of the hadrons with final states in which the transverse momentum distribution of particles is a reflection of the internal structure of the incoming hadrons. By selecting a sample in which the total transverse momentum of events is high enough it is possible to eliminate these processes.

In the region of perturbative QCD the vector meson may be considered a composite object consisting of quarks and gluons. The resulting photon structure function F_2^{VDM} becomes a summation over the vector-meson structure functions F_2^V weighted with the appropriate coupling factor.

$$F_2^{VDM}\left(x,Q^2\right) \;=\; \sum_{V=\rho,\omega,\phi}\left(\frac{e}{f_V}\right)^2 F_2^V\left(x\right) \tag{1.20}$$

where the vector couplings are deduced from the electric charge coupling to constituent partons:

$$\frac{e}{f_\rho} \;=\; \frac{1}{\sqrt{2}} \tag{1.21}$$

$$\frac{e}{f_\omega} = \frac{1}{\sqrt{18}} \tag{1.22}$$

$$\frac{e}{f_\phi} = \frac{1}{\sqrt{9}} \tag{1.23}$$

The vector meson structure functions are unmeasured but may be inferred from those of the π^- assuming isospin and flavour independence.

$$F_2^{\rho^0}(x,Q^2) = F_2^{\pi^0}(x,Q^2) = F_2^{\pi^-}(x,Q^2) = x\left(\tfrac{4}{9}f_{\overline{u}|\pi^-} + \tfrac{1}{9}f_{d|\pi^-}\right) = \tfrac{5}{9}x f_{\overline{u}|\pi^-} \tag{1.24}$$

1.3.3 The Quark Parton Model (QPM)

The Quark Parton Model speculates that the photon may branch into virtual quark-antiquark pairs with a rate and structure predicted by QCD. This can only lead to reliable predictions when the virtuality scale is large enough to apply perturbation theory. Indeed for large enough Q^2 in the next to leading log approximation the structure function, F_2^{QPM} is given by the formula

$$F_2^{QPM} = a(x)\ln\frac{Q^2}{\Lambda^2} \tag{1.25}$$

where $a(x)$ is a calculable function of x and Λ is a parameter introduced into the running coupling constant, α_s, to characterize the scale at which binding occurs. This running is described by

$$\alpha_s(Q^2) = \frac{12\pi}{(33-2n_f)\log(Q^2/\Lambda^2)} \tag{1.26}$$

where n_f denotes the number of quark flavors. As Λ is the only unknown in the structure function equation it was hoped that measuring F_2^γ would accurately determine this important parameter [14]. Unfortunately a lack of data at sufficiently high Q^2 scales and the predominance of the hadronic VDM component have scuppered these hopes. In fact, higher order corrections reveal a singularity in the QPM prediction which must be cancelled by the VDM contribution.

1.4 Resolved Processes

Although VDM and QPM provide theoretical frameworks for generating parton distributions in the photon their contributions are in practice indistinguishable.

Instead all processes in which the partonic nature of the photon may be resolved are classified together. The resulting resolved photon structure function, F_2^γ, is a superposition of those arising from the VDM, F_2^{VDM}, and QPM, F_2^{QPM}, scenarios.

$$F_2^\gamma = F_2^{VDM} + F_2^{QPM} \tag{1.27}$$

Photon and proton structure functions differ in some important features. Firstly the evolution of F_2^γ with Q^2 depends not only on the Altarelli-Parisi Equations but also the Q^2 dependence of the QPM contribution. This leads to a rise in the structure function with Q^2 at all values of x.

The uncharged gluon distributions cannot be measured in DIS leading to large uncertainty. In the proton a summation over all momenta distributions weighted by the momenta must return the original proton momentum providing a valuable constraint on the gluon distribution. A similar summation in the photon case yields only a fraction of the original momentum corresponding to the probability of photon fluctuation into a hadronic state. This is poorly determined and hence the photon gluon distribution may vary enormously.

1.5 Parameterisation of Structure Functions

In practice, structure functions have been measured across a broad range of x and Q^2 in experiments with widely varying statistical and systematic errors. When fitting these data it is usual to select a reference scale, Q_0, at which some appropriate function of a number of parameters is chosen. Either the function is evolved, using the Altarelli-Parisi Equations, to the Q^2 scale of the data or the data are evolved to the reference scale whereafter a fit is performed to determine the parameters. In areas, such as very low x and low Q^2, where data are absent, the evolution equations must be used.

In order to demonstrate the x and Q^2 ranges accessible in this study, I have plotted in Figure 1.6 and Figure 1.7 the values selected by the simulation after all cuts were applied. In this study the MRSD0 proton and LAC2 photon structure functions (discussed in sections 1.5.1 and 1.5.2) were used with a QCD cutoff

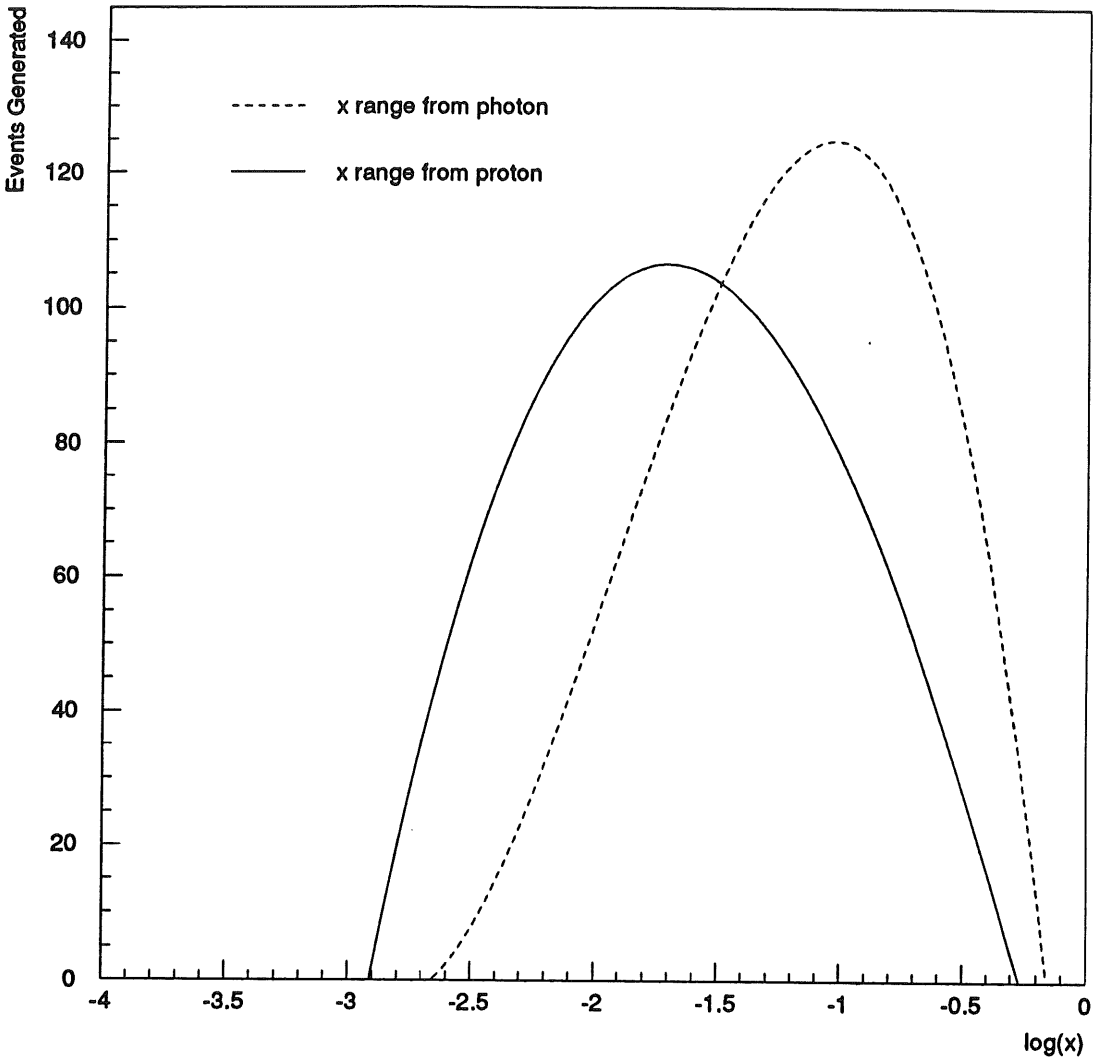

Figure 1.6: Photon and Proton x distributions for selected events

parameter, P_T^{min}, of 2GeV/c. The Q^2 scale used was the square of the transverse momenta of partons emerging from the hard subprocess.

1.5.1 Review of Parameterisation Used

I have used the parameterisations of Martin, Roberts and Stirling [6] which are fitted to data from DIS of electrons and neutrinos from hydrogen, deuterium and iron targets. The data were supplied by the EMC, CDHSW and CCCFRR collaborations. They use a reference scale, Q_0^2, of 4GeV^2. The gluon distribution is described by the function

$$xG(x,Q_0^2) = A_g x^{\delta_g}(1-x)^{\eta_g}(1+\gamma_g x) \tag{1.28}$$

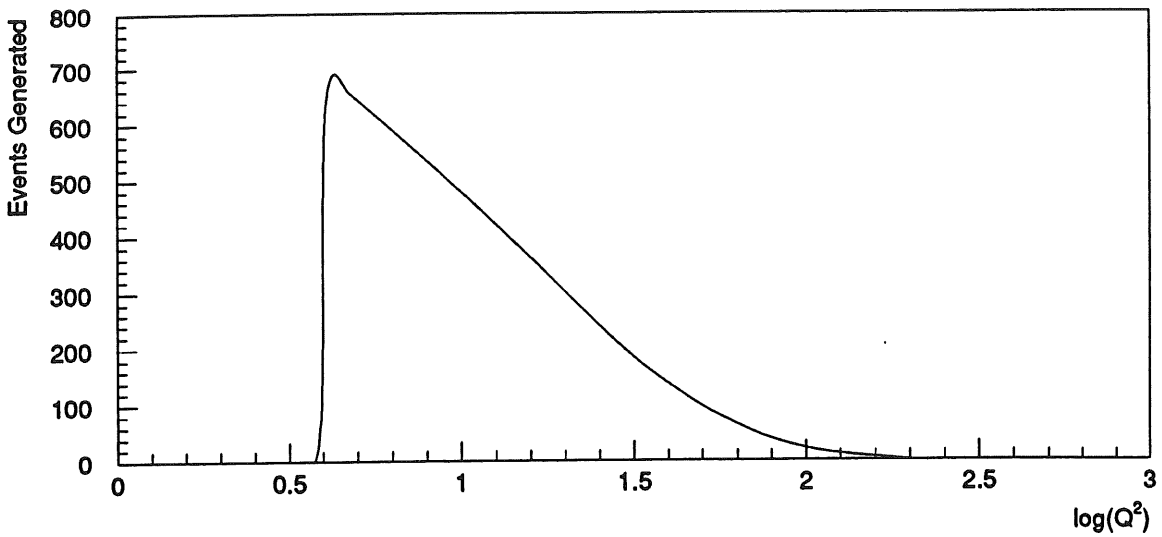

Figure 1.7: Q^2 range for selected events

MRSD0	$A_g = 2.72$	$\delta_g = 0$	$\gamma_g = 0$	$\eta_g = 5.1$
MRSD-	$A_g = 0.315$	$\delta_g = -0.5$	$\gamma_g = 12$	$\eta_g = 5.1$

Table 1.1: Parameters of the gluon structure functions in the proton

Reflecting the difficulty of extrapolating to lower x values, a number of different predictions for the behaviour of the gluon structure function have been tried. Within this study I make use of the gluon parameters as shown in Table 1.1.

In Appendix B these distributions have been plotted as a function of the logarithm of x for a Q^2 of 5GeV^2.

1.5.2 Photon Structure Function Measurements

Since it cannot be derived from theory, F_2^γ must be measured directly. This has been done in electron-positron colliders. One of the leptons radiates an on-shell photon from which the second lepton scatters in a manner entirely analogous to DIS. The scattered electron determines Q^2 but not x as the initial momentum of the on shell photon is not known. To fix this one must also measure the mass of the final hadronic system, W. This is not easily done since it requires a good coverage of the available phase space by the detector. Remnant particles of the photon are generally moving along the beam pipe and cannot be detected. It therefore requires

LAC1a	$C_g = 0.01$	$D_g = -0.5$	$E_g = 1$
LAC2	$C_g = 35.3$	$D_g = 0.0$	$E_g = 17.4$

Table 1.2: Parameters of the gluon structure functions in the photon

careful understanding of detector systematics to extract a structure function.

1.5.3 Parameterised Photon Structure Functions

I have used the parametrisation of Levy, Abramowicz and Charchula [15]. These used functions of 12 parameters to describe the parton density of the four lightest quark flavours and gluons. The initial Q_0 scale was set at 4GeV and the QCD scale parameter, Λ, assigned a value of 0.2GeV. The 51 data points, from the colliders PETRA, PEP and TRISTAN, cover a Q^2 range up to 73GeV^2. The gluon structure function was defined to be,

$$xG(x) = C_g x^{D_g} (1-x)^{E_g} \tag{1.29}$$

where C_g, D_g and E_g are the parameters to be determined. Leaving all three free produces a very extreme structure function which approaches $x^{-0.34}$ as x goes to zero (LAC1) whilst setting D_g to zero makes $xG(x)$ tend to a constant (LAC2). Since the gluon distribution is poorly constrained a more moderately rising function, has been substituted (LAC1a) as the default choice in H1 simulation.

1.6 Initial and Final State Shower Development

In addition to the basic process of parton-parton scattering which generates 2 jet events, there are higher orders in QCD, which describe the emission of further gluons or partons. These give rise to events with 3 and 4 jet topologies and serve to increase the intrinsic transverse momentum of the hard scatter. In principle, some of the higher order matrix elements are calculable, although in practice this is extremely difficult and not directly suited to Monte-Carlo techniques. Instead a scheme of initial and final state showers [16, 17] has been used which only approximates interference effects and ignores helicity states.

The scheme allows the splitting of a parent parton into 2 daughters with the possibilities $q \to q\gamma$, $e \to e\gamma$, $q \to qg$, $g \to q\bar{q}$ and $g \to gg$. For each possibility the probability $P_{a\to bc}(z)$ of splitting is defined as a function of z, the energy fraction taken by daughter b. Final state showering commences with the partons emerging from the hard subprocess and uses the parton mass as a virtuality scale by which emissions are ordered. Monte-Carlo techniques are used to select the mass and energy fraction of an emerging parton. The daughters then become prospective parents until a cutoff virtuality is reached. In the case of initial state radiation the process runs in reverse where the highly virtual hard scattering partons are known and the parent parton energies must be devised. Because the squared masses involved in initial state showers are negative whilst those of final states are positive, they are often referred to as spacelike and timelike showers.

Although the direction of emitted partons is sharply correlated with the direction of those interacting, and thus generally preserves the jet structure, the transverse components can add several GeV to the transverse momentum of the hard scatter system. This adds to the difficulty of kinematical reconstruction.

1.7 Hadronisation

Although QCD is thought a complete theory of strong interactions it is so far incalculable outside the perturbative region. Hence the process of evolving a parton skeleton into an event of colourless leptons and hadrons must be phenomenological. A string fragmentation scheme [18] has been used throughout. This realises the proposed energy tube of self interacting gluons which connects separating quarks as a 'massless relativistic string' of energy density 1 GeV/fm. This has the advantages of producing linear confinement, unambiguously determining the colour relations and satisfying Lorentz Invariance. Quark-antiquark pairs are formed by quantum tunneling causing the string to break up and generating equal and opposite momenta transverse to the string direction. Only the light quarks u,d and s are produced in the ratio 1:1:0.3, since the other quarks are heavily suppressed by their mass.

In an independent process the quarks are paired into pseudoscalar or vector

mesons in a ratio of 3:1. Mesons with non-zero angular momentum are heavily suppressed. Baryons are also produced by assuming that the quarks have a given possibility of becoming the corresponding anti-diquark pair after making adjustments for the new masses and further suppressing strangeness.

1.8 The Photon Flux

The momentum distribution of photons from the beam electrons is determined from QED in a manner exactly analogous to the QCD radiation of a gluon from a quark. The probability, p_γ, of an electron radiating a photon with momentum fraction z and transverse momentum P_T is given by the Weizsacker-Williams Formula

$$p_\gamma(z, P_T) = \frac{\alpha}{\pi}\frac{1}{p_T^2}\left(\frac{2(1-z)}{z} + z^2\right) \tag{1.30}$$

Although this formula is in principle only valid for on shell or zero mass photons the correction for electron tagged events with Q^2 less than 10^{-2}GeV^2 has been shown to be less than 0.3% [19].

1.9 Computer Simulation of Physics Processes

PYTHIA version 5.6 [20] has been used throughout as a generator of direct and resolved QCD scattering processes. Most details of its implementation have been described above with specific initialisation settings given in Table 1.3. All production was carried out using the VAX-cluster of the Lancaster HEP Group.

Due to the sharply falling cross section a weighting scheme was used for events generated at the lowest transverse momentum scales. This increases the complications of analyzing distributions as some bins may contain only one or two events with large weights leading to large errors in that bin. This has been avoided in most cases by setting a bin size large enough to accomodate a number of such entries.

PYTHIA 5.6: Initialisation				
Array	Element	Default	Setting	Description
Photoproduction Switches				
MSEL	3	1	0	Enable user choice of subprocesses
MSTP	11	0	1	Enable $e \to e\gamma$
MSTP	12	0	1	Enable resolved photon subprocesses
MSTP	13	1	2	Enable user defined Q^2_{MAX} in $e \to e\gamma$
Kinematic Limits				
PARP	13	25.	0.01	Q^2_{MAX} (GeV^2) in $e \to e\gamma$
CKIN	3	0.	2./3.	P_T^{MIN} (GeV/c)
Contributing Subprocesses				
MSUB	33	0	1	$q\gamma \to qg$ (QCD-Compton)
MSUB	54	0	1	$g\gamma \to q\overline{q}$ (Photon-Gluon Fusion)
MSUB	11	0	1	$qq \to qq$
MSUB	12	0	1	$q\overline{q} \to q'\overline{q}'$
MSUB	13	0	1	$q\overline{q} \to gg$
MSUB	28	0	1	$qg \to qg$
MSUB	53	0	1	$gg \to q\overline{q}$
MSUB	68	0	1	$gg \to gg$
Structure Function Selection				
MSTP	51	1	46/47	MRS_D0 / MRS_D-
MSTP	52	1	2	use PDFLIB proton s.f. library
MSTP	57	1	2	proton s.f. $\to 0$ for $Q^2 \to 0$
MSTP	55	1	300/302	LAC1a / LAC2
MSTP	56	1	3	use PHOPDF photon s.f. library
Photon Intrinsic Transverse Momentum ($k_\perp$)				
MSTP	93	1	5	distribution shape $dk^2_\perp/(k^2_{\perp 0} + k^2_\perp)$
MSTP	99	0.44	0.6	$k_{\perp 0}$ (GeV/c)
MSTP	100	2.	5.	$k_\perp^{MAX}$ (GeV/c)

Table 1.3: Initialisation Settings of the PYTHIA version 5.6 Event Generator

Chapter 2

The H1 Experiment at HERA

Circling the Hamburg Volkspark, at a depth of roughly 40 metres, is a tunnel containing the storage rings of the HERA electron-proton collider, run by the German high energy physics laboratory, DESY. Approval for construction was granted in April 1984 and was successfully completed, with first collisions, in October 1991. The unique lepton-hadron scheme is a complementary addition to the global particle physics program allowing researchers access to a new energy scale in the historically rewarding and fundamental field of electron-proton scattering. Particular goals include mapping the gluon and quark structure of the proton; investigation of photon-proton interactions; searches for new particles; and measurement of electroweak parameters. As well as stringently testing current theories of the construction of matter, the information will be invaluable when analysing data from future colliders such as the LHC.

2.1 HERA: The Electron Proton Collider

The 6.3 km HERA ring [21], inclined at 6mrad for geological reasons, follows very roughly the perimeter of the Hamburg Volkspark, home to HSV (the only football club never to have been out of the German first division). Electrons and protons, cruising at energies of up to 30GeV and 820 GeV respectively, are magnetically guided and focused through individual vacuum pipes, which merge, every quarter turn, to allow head-on collisions. By modifying equipment from

previously active experiments, the injection system was built at minimum time and cost. The machine is intended to operate with 210 bunches generating a repetition rate of only 96 ns between bunch crossings at collision points. This presents a severe challenge in design and running of both the event trigger and data aquisition.

The old electron-positron machine PETRA and its associated preaccelerators are used to prepare electrons before injection into HERA at an energy of 14GeV. They are then "ramped up" to the final 30GeV limit, a figure harshly dictated by synchrotron radiation. This energy loss occurs when the direction of the path of a charged particle is altered, and rises, matched by the financial pressure, in proportion to the fourth power of γ. The radiation diminishes in inverse proportion to the circumference. As the electron beam is bent into conjunction with the proton pipe synchrotron radiation is emitted which could interfere with event measurement or even damage sensitive detectors. The beam pipe in this region is fitted with carefully defined shields to prevent contamination.

The first stage of proton production is a 50MeV linac for negatively charged hydrogen. After being stripped of their electrons the protons are stored in a small synchrotron accelerator, DESY3, before moving on to PETRA and finally HERA with an energy of 40GeV. Having 1840 times the electron mass, radiation is less of a problem allowing the protons to reach 820GeV. At this momentum much larger magnetic dipole fields are required to squeeze the protons into the same tunnel. To this end dipole magnets have been constructed, incorporating recent advances in superconducting technology, with liquid helium cryogenics, and precision engineering to ensure that the coils move less than 20μm despite being subjected to forces of many tonnes. DESY has built the worlds largest helium liquefication plant to supply the needs of the rings and detectors. RF cavities of 52MHz are used at injection to accept the bunches with a second system for bunch compression operating at 204MHz.

HERA presently supports two large comprehensive experiments for the H1 and ZEUS collaborations. Plans for a facility to investigate phenomena with polarized beams are continuing with confidence after 60% polarization of the electrons has been demonstrated.

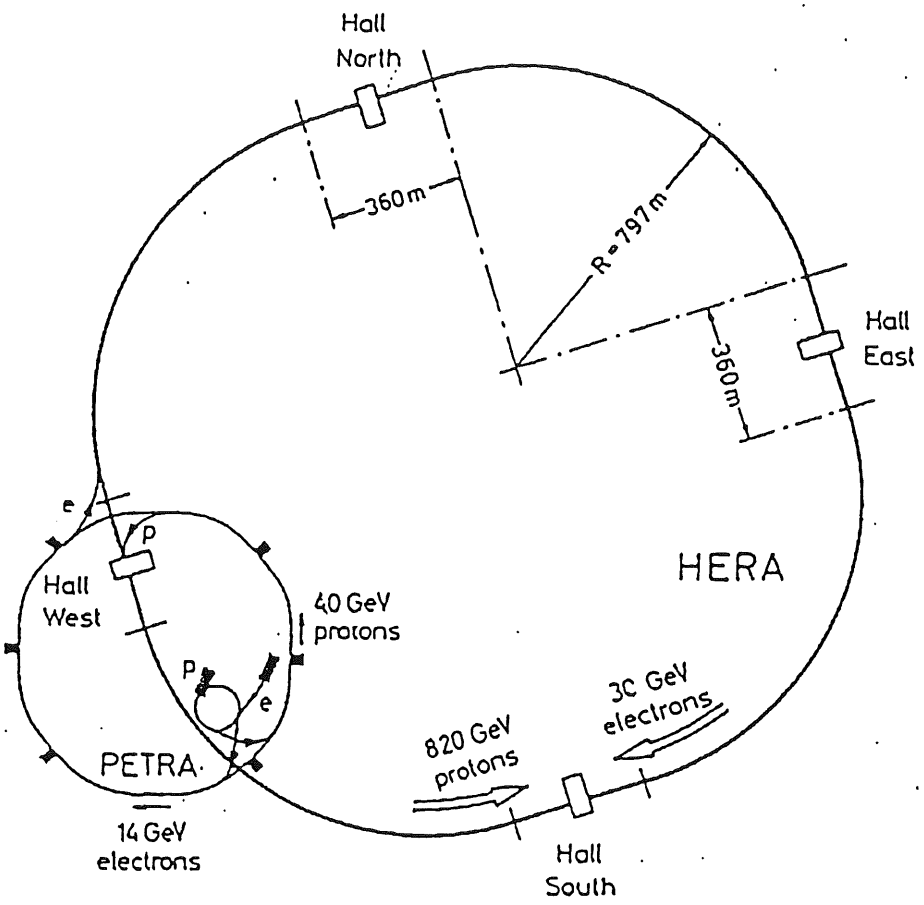

Figure 2.1: The HERA Storage Ring

Technical considerations limited the electrons to 26.7GeV operation throughout 1992, and a problem with one section of beampipe caused rapid deterioration of lifetime for electron currents greater than 3 mA. At various stages the failure of R.F systems allowed the proton bunch lengths to grow to double the required 0.5m size. In 1992 HERA delivered an integrated luminosity of $60nb^{-1}$. For much of the time H1 data logging was not enabled due to periods when H1 was out of operation. This occured, for example, during a quench of the main solenoid or whilst waiting for conditions to stabilise after beam injection before sensitive tracking chambers could safely reach operating voltage. Hence only $36nb^{-1}$ were recorded by H1. Accepting only those runs where all crucial detectors were operating left $25nb^{-1}$.

2.2 An Introduction to the H1 Detector

To visit the H1 detector, one enters the North Hall site at DESY, descends 7 subterranean floors by lift, and then turns a corner into a box shaped cavern with ample height to house the 10m tall detector. Usually it is in beam position hidden behind metres of concrete shielding but, during shutdown periods of HERA, its 2000 tonnes are trundled away from the storage ring and parked in the centre of the Hall for access and maintenance.

In the parked position, before opening the structure, only the iron return yoke is visible. This has a laminated structure, the gaps being instrumented with streamer tubes to tag escaping muons and to catch the tail of energy showers which spill out of the calorimeter. Part of this shell can be drawn away revealing the casing of the superconducting magnet which provides an axial field of 1.2T, uniform to within 3% over the entire tracking volume. The magnet is situated outside the main calorimeter where its material interferes least with energy measurement. Also visible is the shiny dome of the liquid argon cryostat which is shaped like a bullet pointing forward with the charge drilled out to allow access for tracking. This cryostat contains the liquid argon calorimetry comprised of a hadronic part using stainless steel plates and, inside this, an electromagnetic calorimeter using lead plates. These calorimeters cover the front and barrel regions with steadily increasing granularity in the forward direction. The back end of the detector is opened

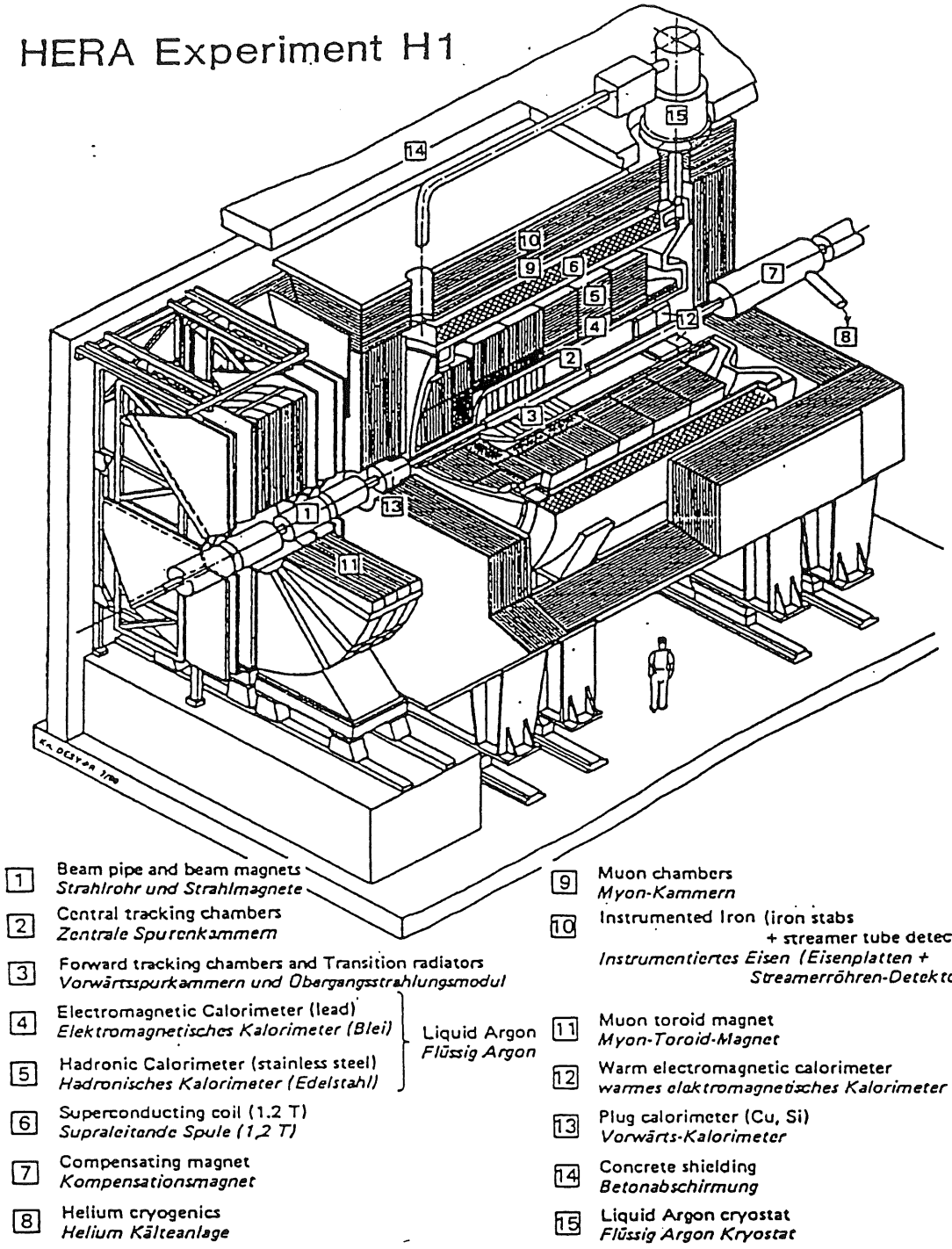

Figure 2.2: Layout of the H1 detector

up and detectors are pulled out from the cavity. First out is the Time Of Flight (TOF) counting system comprising a double layer of fast acting scintillator. This has high time resolution allowing particles from the interaction to be distinguished from background debris of proton interactions with residual gas. Next emerges the Backward ElectroMagnetic Calorimeter (BEMC). It is a lead/scintillator detector read out by wave length shifter bars and photodiodes. Fixed to the front of this are the Backward Multiwire Proportional Chambers (BPC). These are followed by the Central Tracker which usually sits symmetrically about the interaction point. Two Central Jet Chambers (CJC1 and CJC2) with wires running roughly axially are used for track reconstruction with good $r-\phi$ resolution for determining transverse momentum. These are combined with proportional chambers for fast trigger information and Z chambers to aid track reconstruction. Last out of the cavity is the Forward Tracker with a unique geometrical arrangement of wire chambers to cope with the high density of tracks in this region. These are sandwiched together with more Proportional Chambers and transition radiators to allow separation of electrons and pions.

Left behind in the tunnel a little in front of the main detector are the forward muon chambers designed to measure the momentum of emerging muons. In the other direction, at distances of 33 and 100 metres respectively, are electron and photon Cerenkov total absorbtion counters, which form the main elements of the H1 luminosity monitor.

For a more comprehensive guide to the H1 detector a technical report is available [22].

2.3 The Magnetic Field System

The H1 detector magnetic field is provided by 4 superconducting coils with a diameter of 6m, situated outside the Liquid Argon Calorimeters. These generate an axial field of 1.2Tesla which varies by less than 3% over the sensitive tracking volumes [23, 24]. The superconducting material is a niobium-titanium composite bonded in copper and clad in aluminium in order to carry the current and limit heat increases in the event of a quench. This is wound on an aluminium for-

mer supporting the 1.5MPa Magnetic field pressure, and axial forces of over 2000 tonnes.

2000 tonnes of iron act as a return yoke. The iron is laminated and the gaps fitted with streamer tubes, used for tracking escaping muons and detecting energy leakage from the calorimeter.

A superconducting compensation magnet, with a maximum field of 6 Tesla is required to preserve the polarisation of electrons. This also limits the instability of beam particles with small transverse momenta.

2.4 The Tracking Chambers

2.4.1 The Central Tracking Detector

The Central Tracking Detector (CTD) [25] is a cylindrical detector with active volume between -1320mm and 1270mm in z. It consists of the following elements: inner and outer Z-chambers (CIZ and COZ); inner and outer proportional chambers(CIP and COP); and two axial wire drift chambers (CJC1 and CJC2) as shown as a plan view in Figure 2.3 and as a section in Figure 2.4. It is designed to trigger on and measure charged particles between 25 and 155 degrees. The objectives of minimizing multiple scattering and photon conversion dictated the use of the minimal material necessary for mechanical stability.

CJC1, from 200mm to 453.5mm in r, and CJC2, from 527mm to 843mm in r, provide r-ϕ track measurement with 150μm resolution via drift time analysis, and mean z resolution of 2cm from charge division [26]. A gas mixture of $Ar/CO_2/CH_4$ in the ratio 89/10/1 has been used throughout.

Each chamber is segmented into cells running the length of the chamber but radially tilted between 18.6 and 41.2 degrees as a function of r. This tilt partly compensates for Lorentz angle effects but also reduces cross-talk and resolves drift side ambiguities for tracks crossing cell boundaries. This geometry also ensures that many tracks cross the sense wire plane allowing the time at which the track passed to be determined. There are 24 sense wires per cell in CJC1 and 32 per cell in CJC2, each of the wires being separated by a pair of potential wires which

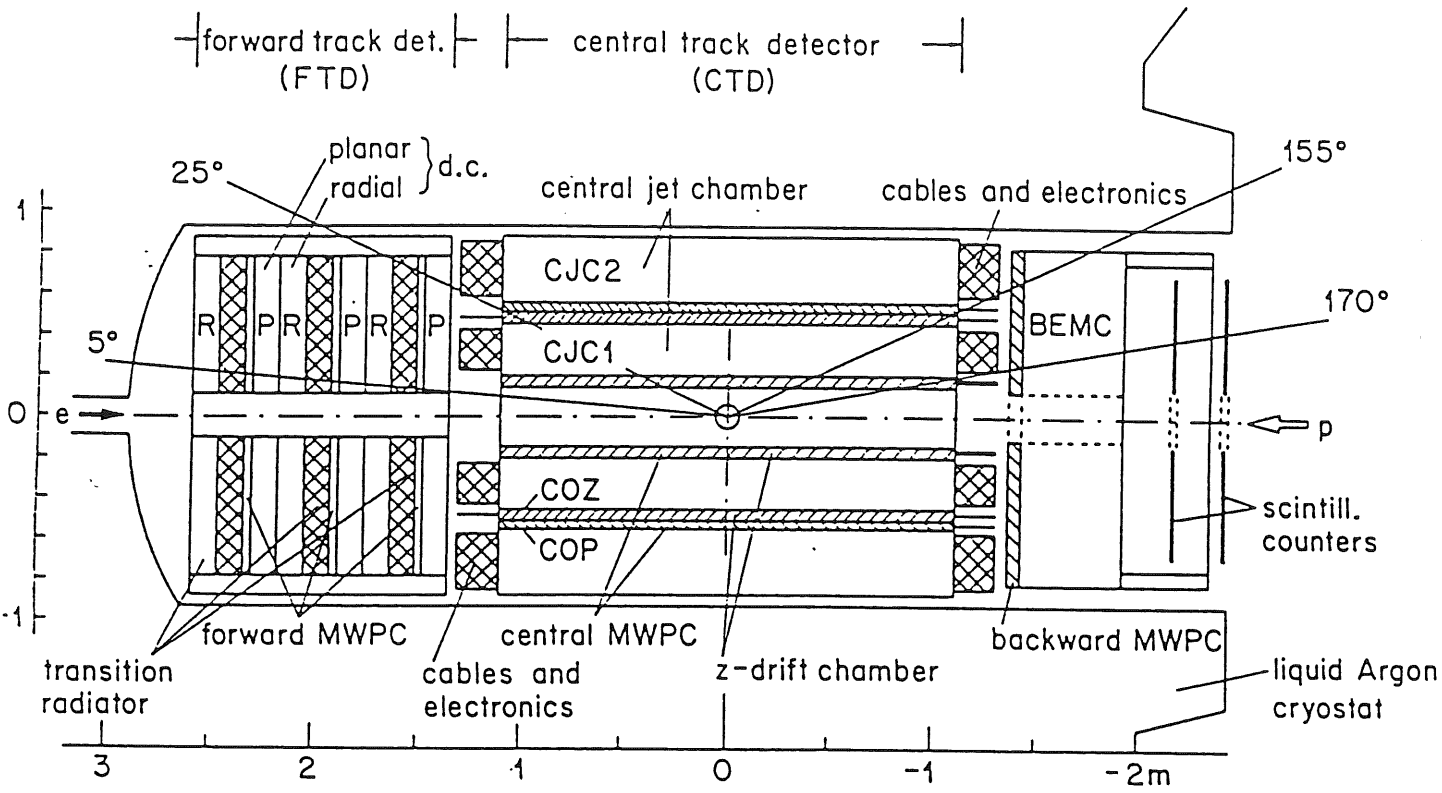

Figure 2.3: Layout of the tracking chambers ($r-z$ view)

shape the field. Maximum drift distance is limited to 51mm by the drift velocity of 35μm/ns and the data aquisition time limit of 1.5μs.

The CIZ, active between 173mm and 193mm in r, and the COZ, active between 456mm and 480mm, are used to improve z-resolution of tracks in the CJC. The COZ is divided into 24 slices of 9cm in z. Each slice is a 24 sided polygon coaxial with the beam pipe. Four sense wires are wound round the polygon to form a conventional drift chamber with drift in the z direction. Charge division allows the ϕ coordinate to be measured with an accuracy of 2cm or 7 degrees. Resolution of the z coordinate varies between 150μm and 400μm as θ changes from 90 to 30 degrees. The CIZ is similar but has only 15 slices and 17 edges to the polygon. One edge is used for read out and cabling. One difference is that the wires in a cell are tilted by 45 degrees in θ in order to follow the track angle. Accuracy is about 320μm in z for track angles between 20 and 170 degrees.

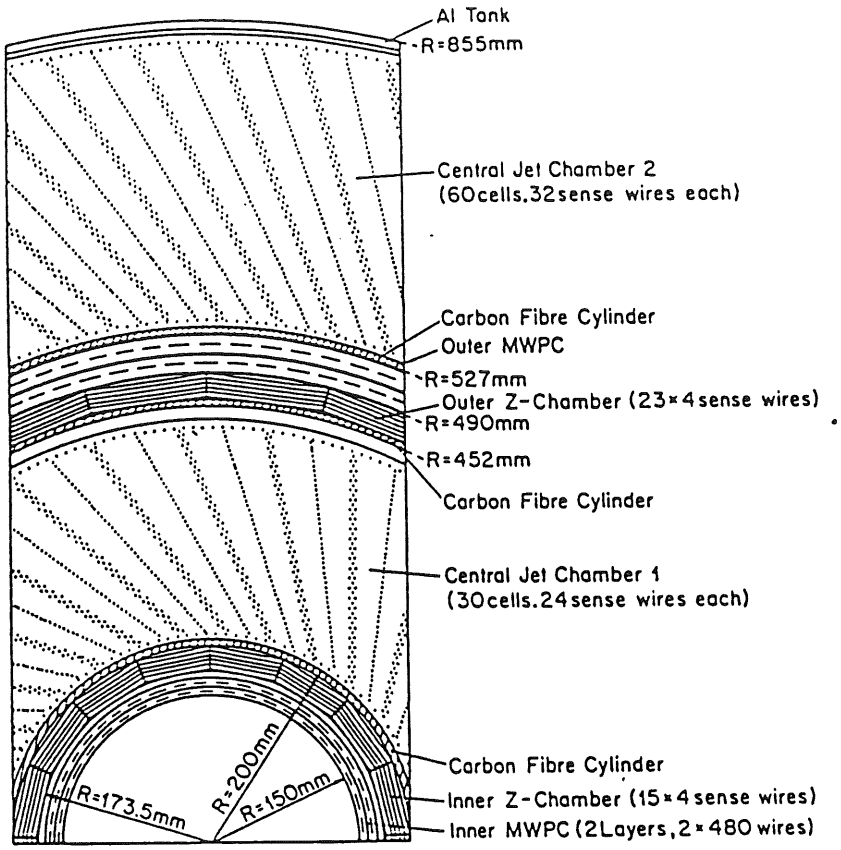

Figure 2.4: Central tracking system, section perpendicular to beam

2.4.2 The Forward Tracking Detector

The Forward Tracking Detector(FTD) covers an angular range between 5 and 30 degrees in θ where proton remnants and large jet cross sections produce a high density of tracks. It combines drift chambers of unique geometry for particle tracking with proportional chambers for triggering and includes planes of transition radiators to allow electron/pion separation. As before, the requirement to minimize the amount of material used and the short time allowed for readout have greatly affected its design. It is constructed of three identical 'supermodules' each of which sandwiches together, in increasing z: a planar chamber, proportional chambers, material for transition radiation and finally radial chambers.

The planar chambers are formed from three identical layers each rotated by 60 degrees in ϕ from the previous layer. Rectangular drift chambers of width 5.7cm are stacked parallel to one another inside a layer and truncated to fit within the inner and outer radii. The wires are read out at one end allowing only the coordinate perpendicular to the wires to be determined. This is measured with

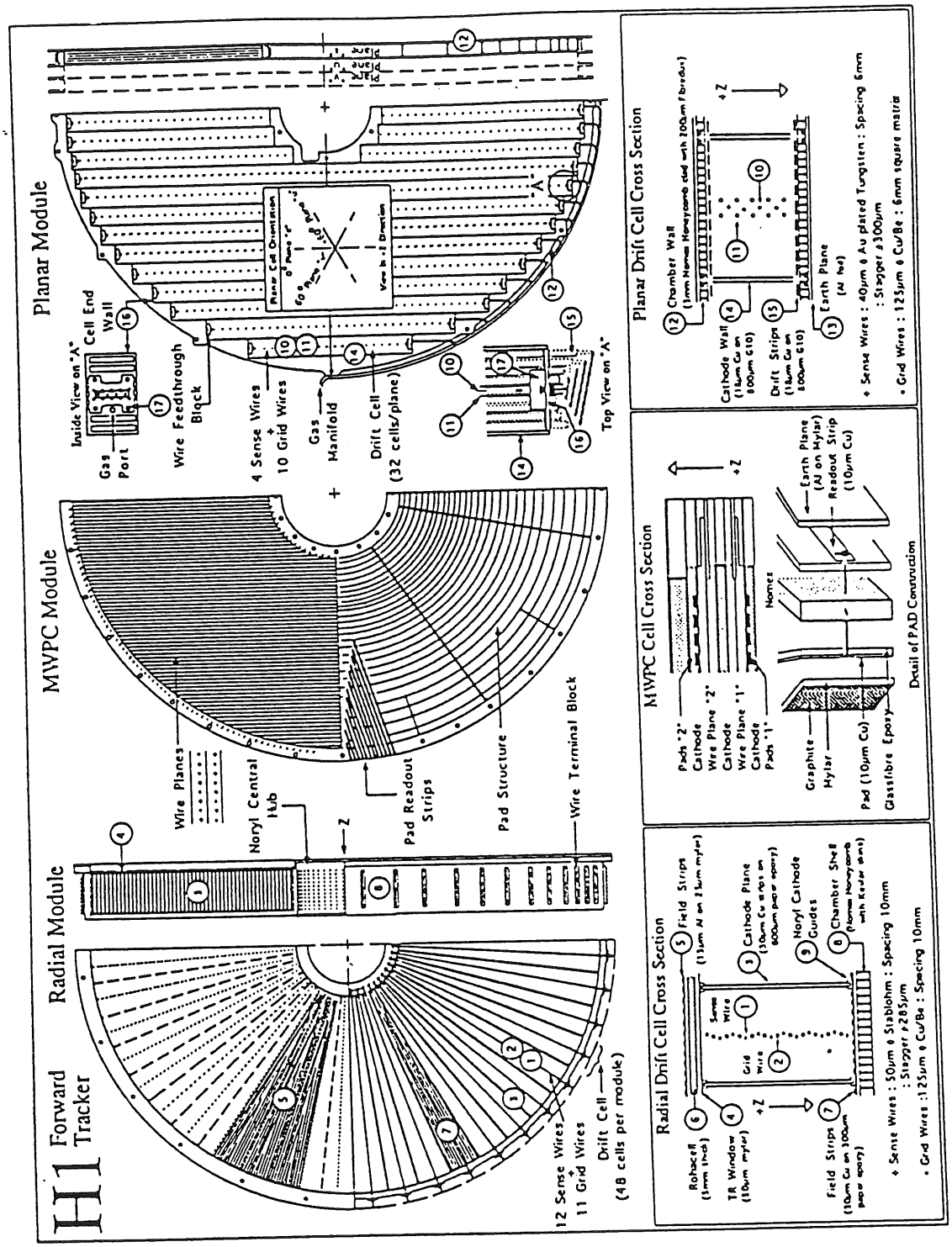

Figure 2.5: Construction of the Forward Tracker

an accuracy of 150μm. Thus one layer cannot give hits along the path of a track but only defines a plane in which the track moved. The intersection of planes from three layers angled at 60 degrees to one another allows the path of a track to be determined, but only after the numerous false intersections arising have been discarded.

The radial chambers are wheels divided into 48 segments. Each segment forms a drift chamber 12 wires deep in z. This novel arrangement provides increased wire density at smaller radius where the density of tracks is greatest. The segments are paired together such that the wires run from the outside of one wedge to the hub and then from the inside of another wedge out again to the rim. This allows simple access to read out both wire ends enabling charge division for determination of the r coordinate of hits with 2cm resolution.

The transition radiator is 7cm thick and consists of many layers of polypropylene sheets. On traversing this a charged particle radiates photons with an intensity proportional to its γ factor. A mylar window allows these photons to enter the radial chambers where they may be detected as increased charge deposition on the first wires.

2.5 The Calorimetry

2.5.1 The Liquid Argon Calorimeter

Providing the calorimetry between polar angles of 4 and 153 degrees is a liquid argon calorimeter with an outer hadronic section (HAC) of stainless steel plates and an inner electromagnetic (EMC) section of lead. With DIS firmly in mind, the design has maximised electron/pion separation and provided increasing granularity in the forward region. The depth ranges between 20 and 30 X_o in the electromagnetic part and from 5 to 8 λ in total. There is approximately $1X_o$ of dead material traversed before reaching the calorimeter.

The calorimeter has an eightfold segmentation in ϕ, with radial cracks in the EMC and non-radial cracks in the HAC. Polar segmentation is greatest in the forward region and decreases with increasing polar angle. Plates are mounted

vertically in the forward region and parallel to the beam axis in the barrel region. Readout boards are mounted directly onto the lead plates but held in the gaps of the steel construction. Systems built into the design indicate signal attenuation due to impurities in the argon at less than 0.5% per year. The electronics readout is also constantly monitored using test pulses.

Calibration was carried out at CERN using test beams of electrons from 5 to 80GeV and pions from 3.7 to 205 GeV. In each case one module of each shape was tested in all possible orientations including scans across cracks. Detailed Monte-Carlo simulation is then used to provide final corrections for variations between stacks and effects of dead materials. The details of reconstruction are described in section 3.2. The overall resolution σ/E for electrons is approximately $12\%/\sqrt{E}$ and for pions $50\%/\sqrt{E}$. These energy scales have been verified in situ to within 8% using cosmic muons and P_t balance of DIS events [29]. A separate study of electrons produced by cosmic muons has provided a resolution σ/E of $20\%/\sqrt{E}$ for electrons with average momentum 1.6GeV/c.

2.5.2 The Backward ElectroMagnetic Calorimeter

The BEMC is a lead/scintillator calorimeter covering a range of 150 to 176 degrees in theta. The sandwich has 49 layers of 2.5mm thick lead and 50 layers of 4mm scintillator (SCSN38) with read out of each stack provided by two WaveLength Shifter bars WLS and photodiodes. The horizontal depth of 22 radiation lengths amply accommodates the shower depth of 30GeV electrons. The error attainable depends on the shape of the stack, the square stacks being much better than those of other shape around the outside edge and close to the beampipe.

Although much calibration work has been done using test beams, final calibration occurred in situ using electrons from low Q-squared neutral current DIS events. These have an energy distribution sharply peaked at the electron beam energy.

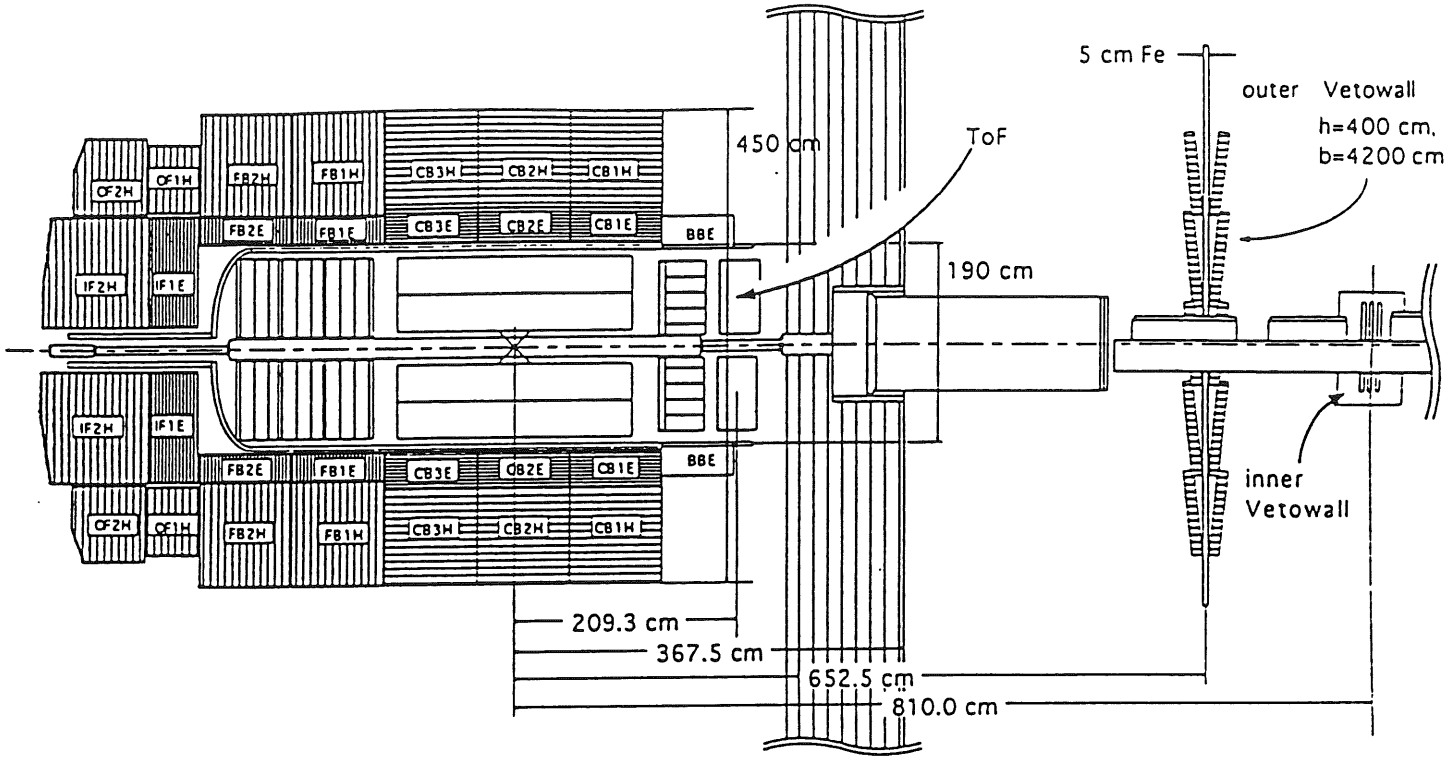

Figure 2.6: Configuration of the Calorimetry and Veto Systems

2.6 The Trigger System

2.6.1 The Multi-Wire Proportional Chambers

There are four sets of MWPC's in the H1 detector: Central Inner and Outer Proportional chambers (CIP and COP) located concentrically inside CJC1 and between CJC1 and CJC2; the Forward Multiwire Proportional Chambers incorporated in each supermodule of the Forward Tracker; and the Backward Proportional Chamber fixed to the front face of the BEMC. These are designed to respond to charged particles within the 96ns bunch crossing time and provide information for Trigger Level 1. Combining information from the CIP, COP and the FPC's allows crude reconstruction of the event vertex and is a powerful physics signal. CIP and COP are cylindrical detectors each with 2 chambers in r divided into cathode pads 60 times along their length and 8 times in ϕ with anode wires running axially inside a gap of 3mm. The anode wires are not instrumented, the fast signal provided by the pattern of pads hit. Voltages induced on the cathode pads by electrons drifting

away from ionised particles are fed along aluminium wave guides to preamplifiers at the -z end. A base width time resolution of 76ns has been measured using cosmic muons.

2.6.2 The Time-Of-Flight Counter and Veto Walls

The dominant source of background arises from proton interactions with residual gas or the vacuum pipe.These produce particles outside the beam pipe travelling alongside the proton beam. These hit the scintillation walls at the same time as the protons pass by in the vacuum pipe. Particles from collisions at the interaction point are delayed by the time taken for the protons to travel there from the TOF position plus the time taken to return. Scintillation walls placed in the backward direction use fast timing information to distinguish background from genuine interaction fragments. These provide the most powerful background suppression at trigger level 1 vetoing 99% of positive signals from other detectors.

The Time-Of-Flight (TOF) system is situated behind the BEMC 2m from the interaction point providing a nominal 13ns separation between accept and reject signals. Two 3cm walls of NE102A plastic scintillator are read out using photomultiplier tubes mounted parallel to the field axis and logically OR-ed to define a crossing time. The device has an overall resolution of 4ns.

At 6.5 and 8.1 metres from the interaction point are found the large outer veto wall and the small inner veto wall. The large outer wall has an area of $20m^2$ and provides cover for the whole detector from highly penetrating muons. The smaller wall is designed to be as close to the beam pipe as possible to reject particles emerging at small angles.

2.7 The Luminosity Monitoring System

Two arrays of Cerenkov total absorbtion counters, using KRS-6 monocrystals read out by photomultipliers, form the H1 luminosity monitor. One is placed 33 metres from the interaction point in the -z direction and acts as an 'electron tagger'. It detects electrons in an energy range between 1/5 and 4/5 of the full beam

energy and a polar divergence less than 5mrad corresponding to a maximum Q^2 in photoproduction events of 0.01GeV^2. The electron paths are bent by the first set of dipole magnets and leave the beam pipe through a small exit window. The second array is placed 100m from the interaction point in the -z direction and detects photons which exit the beam pipe as it bends upward. It is fronted by $2X_0$ of lead and $1X_0$ of a water Cherenkov counter to shield against synchrotron radiation and to veto charged particles. It is shielded from behind by 2 meters of iron to avoid proton beam halo. Each array has an energy resolution of $1\% + (10\%/\sqrt{E})$. The overall energy scale is calibrated by using the predominant bremsstrahlung events where the energy deposits in electron and photon calorimeters should sum to the electron beam energy. These events are used for luminosity monitoring as they provide a process with a large cross section precisely calculable using QED theory and with a clear signature.

2.8 Monte-Carlo Detector Simulation

Simulation of detector response has been handled throughout by the H1SIM program running in the 'fast' mode.

For the calorimeter this uses a simplified geometry where the alternating absorber and read-out materials are replaced by a homogeneous mixture. Hadronic showers are simulated using Monte Carlo techniques following the shower development down to low cut-offs. For electromagnetic showers, which have generally higher particle multiplicities and hence more reliable statistical properties, a parameterization of the shower development is used. Where showers extend across cracks the parameterized development is halted and, after corrections for dead materials, a new shower is initiated in the neighbouring block. This scheme decreases processing time by an order of magnitude without significantly deteriorating those features essential for analysis, as demonstrated with electron and pion test beam data [27].

In the case of wire chambers simulation begins at the level of hits rather than charge deposit. A charged particle passing a wire creates one hit with position smeared according to detector resolution. In cases of faulty wires which were

insensitive or broken wires which disrupted all the wires in a particular cell, a 'dead wire map' was used.

Chapter 3

Event Reconstruction and Detector Simulation

3.1 Track Reconstruction in the Central Tracker

The density of hits along a track in the Central Tracker is relatively high allowing a very simple reconstruction algorithm to be employed. All sets of three adjacent wires are checked to see if they contain hits which might be linked together. Thereafter connecting sets of three are linked to form chains. These chains are checked for kinks before attempts are made to identify chains common to a single track. The ambiguity arising from indeterminate drift sign can normally be resolved by joining tracks across cell boundaries. All of the wire planes and cells are offset to the radial direction causing the majority of tracks to traverse them along its path. Tracks crossing the wire plane allow a t_0 to be calculated for the event, which determines at which bunch crossing the collision occurred. The biggest problem is probably due to the error in the z measurement of each track which makes it difficult to match hits in the z-chambers with particular tracks in the CJC.

As shown in Figure 3.2, the uncertainty, ΔP_T, in the measurement of the track transverse momentum varies in proportion to its square.

$$\Delta P_T = k P_T^2 \tag{3.1}$$

with constant of proportionality, k, equal to 0.01 for tracks with linked segments in both chambers and 0.08 for those which were reconstructed in the inner part

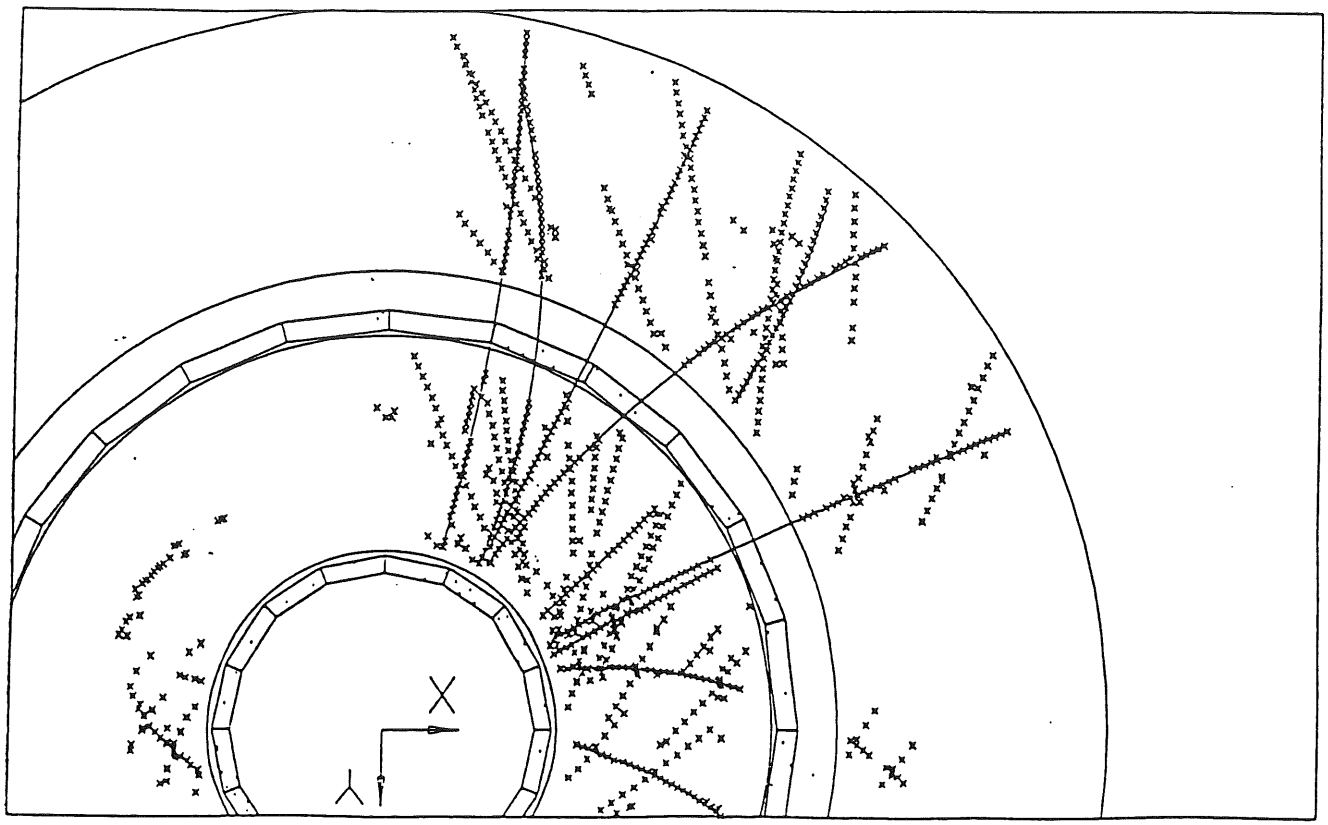

Figure 3.1: Reconstruction in the Central Tracker

only.

As a further investigation I simulated 500 events with only one positive pion with energies of 0.5,1,2,3,4 and 5 GeV. These had the same characteristics as described above. I noted that for each set there was a 4% probability that a track would be missed and also a 4% probability that the track would be split. I believe that this is caused by the poor z-resolution of the tracker.

3.2 Clustering in the Liquid Argon Calorimeter

Each calorimeter cell generates electronic noise, σ_{noise}, of between 10 and 30 MeV mainly depending on the capacitance and hence the size of the cell. To suppress this, only cells with signal greater than $+4\sigma_{noise}$ are kept and act as seeds such that any cells touching these with signal greater than $+2\sigma_{noise}$ are also kept. In order to provide noise compensation, cells with negative energies below $-2\sigma_{noise}$ and $-4\sigma_{noise}$ are also retained although the $-4\sigma_{noise}$ cells are not treated as seeds.

The clustering concentrates on separating deposition from electromagnetic and hadronic showers rather than the combination of one hadronic shower into one

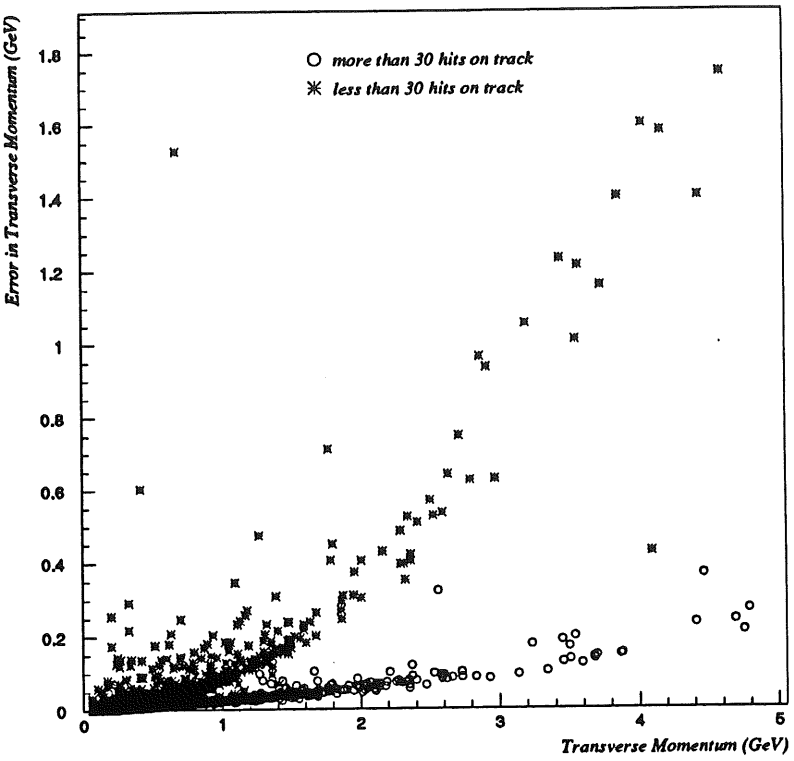

Figure 3.2: Accuracy of measurement of Transverse Momentum

cluster. This is motivated by two requirements: identification of electrons in DIS; and the need to give separate energy weighting for electronic and hadronic showers in a non-compensating calorimeter. Electromagnetic clusters are identified by the fraction of energy deposited in the first layer or in the four most energetic cells. Links are not made across the HAC/EMC border if an electromagnetic shower has been identified. The clustering is carried out in 2 stages. Firstly a 2D search combines connected regions longitudinally within a module and separates maxima to aid shower identification. Secondly a 3D search is made combining connected 2D clusters within a module and finally across cracks. Once clustering is complete noise is further reduced by cutting signals more than 50 cm from a 'prominent' cluster defined to have a significance, $\sqrt{\sum (E_i/\sigma_{noise})^2}$ above 8. Corrections are applied for dead material both in front of the calorimeter and within cracks, and clusters are weighted to compensate for the different detector response to hadronic or electromagnetic clusters.

3.3 Track Reconstruction in the Forward Tracker

The software for reconstruction in the Forward Tracker was revised and substantially rewritten during 1992. Due to this a stable reliable version became available only at a late stage in the analysis after a final event sample had been selected. For this reason I have based most of the analysis on the Central Tracking Detector and only used the Forward Tracker to prepare some inclusive distributions.

Reconstruction in the Forward Tracker is based on the planar chambers. These are chambers with parallel wires, 4 deep in the z direction with a slight stagger to assist in resolving the drift sign ambiguity. From hits on the four wires, which determine the drift time and hence the drift distance, it is possible to reconstruct a plane in which a charged particle moved. Each supermodule has three planes. The first plane has vertical wires, the second has wires sloping at 60 degrees and the final plane has wires sloping at minus 60 degrees. No information is gathered relating to the distance along the wire at which the hit occurred so, from the hits in one cell one cannot determine a track path but only a plane through which the track moved. By combining the three offset planes a small segment of a track can be accurately reconstructed. This leads to the problem that two hits may cause four possible intersections which must be untangled to determine the correct configuration of tracks. One method developed for this task is to draw maps which describe the connections between each of the possible intersection points and then eliminating those which have the greatest number of possible connections. These problems become quickly worse as the number of tracks in the Forward Tracker increases. The planar chambers have simple structure which is offset by complicated and CPU intensive software.

Segments thus produced are linked between supermodules by projecting to a midpoint and connecting those which are nearest within a specified cutoff distance. The tracks are projected into the radial chambers where neighbouring hits are picked up in order to more precisely define the track characteristics.

3.4 Analysis Tools

The H1 PHysics ANalysis (H1PHAN) package has been used throughout to handle the data and analyze events. It allows access to tracks and clusters and also provides a number of routines to operate upon them. Both real and simulated data have passed through the same subroutines in order to ensure a consistent approach throughout.

3.5 Selection of 4-vectors

From an early point a decision was taken to limit the major part of the analysis to the central region between 30 and 150 degrees. Although this excludes the greatest part of the cross-section, it has advantages in simplifying the technical and theoretical interpretation of the data.

Due to the innovations involved in the Forward Tracker it was clear that a considerable period of running would be required to produce well understood and convincing reconstruction. The area requiring linked tracks between the two trackers would be particularly insecure. Hence the use of Central Tracker tracks backed up by information from the electromagnetic calorimeter seemed a wise choice. It could at least be treated homogeneously.

The poor understanding of how the proton remnant might behave also motivated this decision. After a quark from the proton has been knocked out, the remaining pieces of proton disintegrate, creating a forward moving proton remnant jet. This is likely to be measured in the Forward Tracker. The central region would be the cleanest area for selecting the hard processes of greatest interest.

3.5.1 Central Track Selection

The following cuts were used to select central tracks:

- θ between 30 and 150 degrees
    - ◇ restricts the tracks to be well contained by the coverage of the central tracker

- the start of a track less than 30cm from the central axis
    - ◇ This condition excludes tracks starting in the outer barrel of the CJC. Tracks segments originating from one particle which have been reconstructed separately in the inner and outer chambers but failed to be correctly linked are thus not double-counted.
- Track linked to the vertex
    - ◇ This condition helps to ensure the track isn't spurious and neglects fragments from decaying particles which could be counted twice; once from parent and again by the daughter
- at least 10 hits along the track
    - ◇ There are a possible 24 wires crossed in the inner barrel of the CJC and 54 in both chambers together.
- $\Delta P/P$ less than 0.5 for Pt distributions only
    - ◇ This cut ensures that the track momentum is reasonably well determined. This level of uncertainty is reached when the transverse momentum exceeds 50GeV/c for tracks in both chambers but only 6.25GeV/c for those reconstructed in the inner part only.
- Pt greater than 0.1GeV/c
    - ◇ Particles with a lower transverse momentum spiral inside the jet chamber
- ϕ cut between 3.239 and 3.927 radians for positive tracks and between 2.945 and 3.632 for negative tracks.
    - ◇ During the run period two broken wires caused the loss of tracker segments leading to a large inefficiency in these ranges. The effects are shown in Figure 3.3

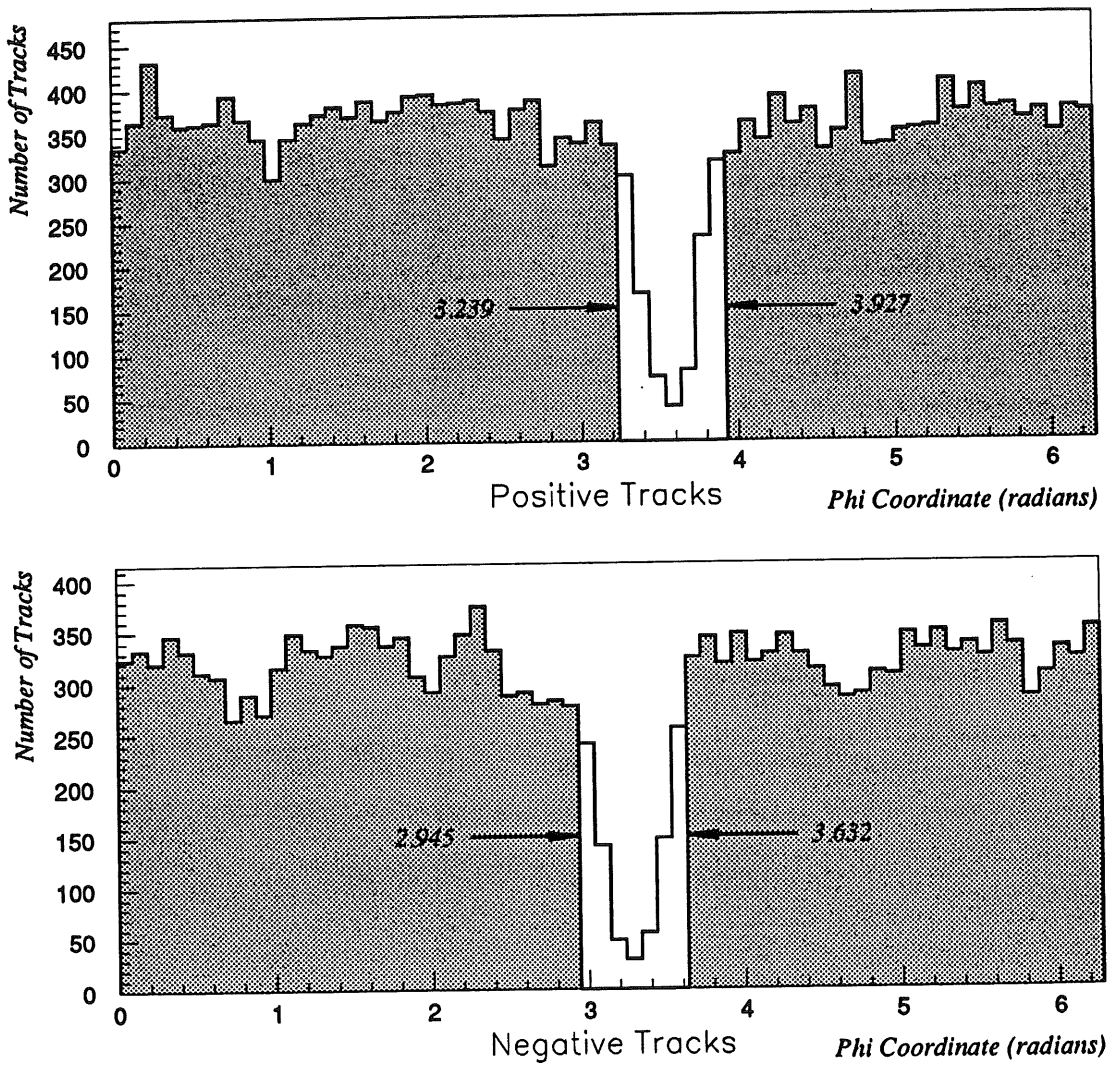

Figure 3.3: Azimuthal distribution of tracks showing cuts used

3.5.2 Forward Track Selection

The cuts used in selection of tracks in the forward tracker were:

- θ between 5 and 25 degrees
    - ◇ avoids the crossover region between the forward and central trackers where reconstruction efficiency is particularly difficult to estimate and where the linking of forward and central tracks would require investigation.
- at least 1 planar segment linked to the track
    - ◇ One planar segment is enough to ensure a well determined track position and momentum measurement.
- Pt greater than 0.1GeV/c
    - ◇ Particles with a lower transverse momentum spiral inside the jet chamber
- Track linked to the vertex
    - ◇ This condition helps to ensure the track isn't spurious and neglects fragments from decaying particles which could be counted twice; once from parent and again by the daughter

3.5.3 Cluster selection

To study the effects of background noise in the calorimeter I have studied 1000 events taken using random triggers during normal operating conditions. The raw distributions of clusters in θ and transverse momentum are shown in Figure 3.4. The forward region has higher segmentation leading to smaller capacitances but a greater density of cells. After applying the 2σ noise cut there are more cells remaining in this region, although with lower signal than those in the barrel and backward parts of the calorimeter. The distribution of transverse momenta falls exponentially. There are no studies of the performance of the calorimeter below the

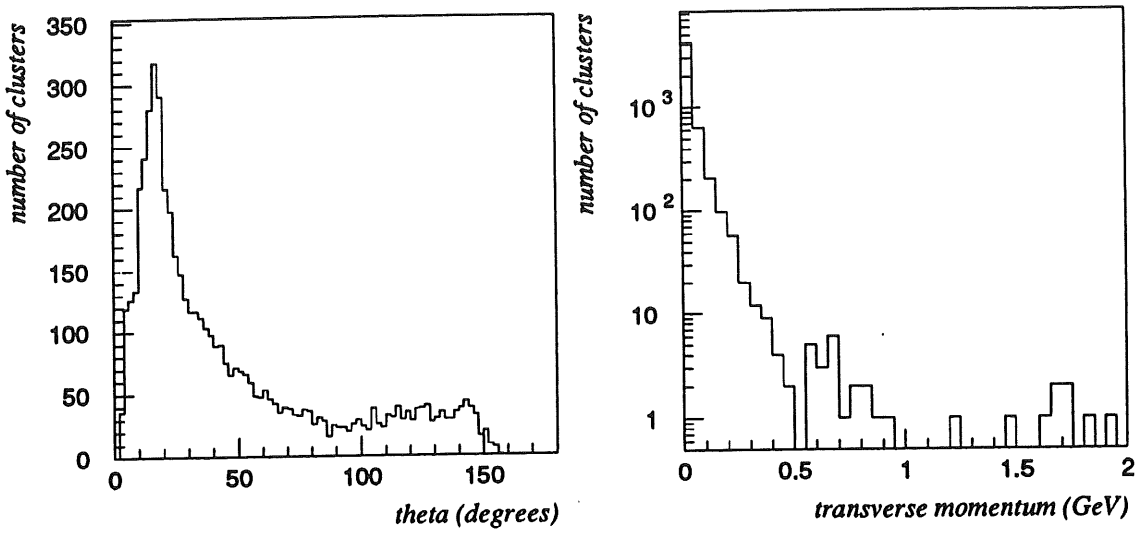

Figure 3.4: Cluster distributions in randomly triggered events.

interaction of 0.6GeV electrons. I have decided to place a cut at 0.6GeV, leaving only 1 noise cluster every 10 events, and hope thereby to pick up as much signal as possible.

The selection cuts for clusters were therefore:

- θ between 30 and 150 degrees
  - ◇ restricts analysis to the region covered completely by the central tracker
- transverse momentum of cluster greater than 0.6GeV
  - ◇ excludes the worst of the background noise clusters picked up after the 2σ cut.

3.6 Linking Tracks and Clusters

For one of the energy flow schemes studied, it was necessary to identify electromagnetic clusters which were associated with charged tracks in order to eliminate them. For this purpose an electromagnetic cluster was defined as any cluster with greater than 90% of its energy deposition in the electromagnetic part of the calorimeter.

The distance between the projected impact point of a track with the calorimeter and the centroid of cluster was used to determine which sets should be linked.

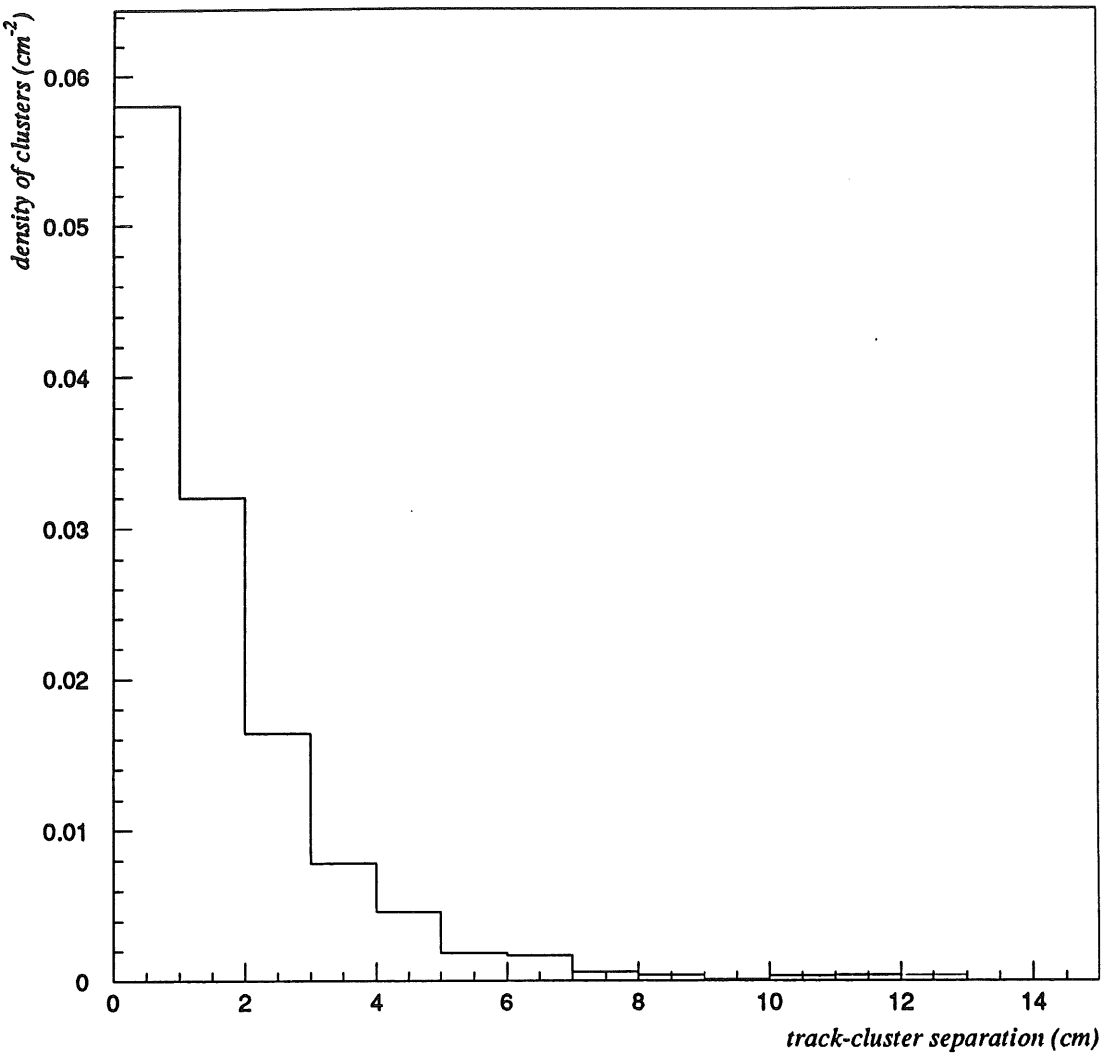

Figure 3.5: Cluster density falls as the distance from the impact of a track with the calorimeter increases

Using the samples of 5GeV pions I had previously generated I plotted the falling density of clusters (Figure 3.5) as a function of the separation. I felt that this plot suggested cutting clusters within 5cm of a track leaving less than 1% probability of picking up any energy twice. I compared this possibility with the II1 default of 15cm by using the method described in section 7.1.4. I found the II1 default specification to give a slightly better resolution for total transverse momentum and hence I have used this throughout.

Chapter 4

Systematic Errors

4.1 Wire Chamber Errors

The main sources of systematic error arising from the Central Tracker are connected with the efficiency of reconstructing tracks and the possibility of tracks being split which results in a double contribution. In fully reconstructed simulation, using events generated with one track, 4% of tracks were missed and also 4% double counted, with little variation between 0.2 and 5GeV. I assume these figures to represent the order of magnitude of uncertainties in the detector and hence assume an 8% systematic error for distributions of inclusive particles. I have been cautious in estimating this error in the light of the limited experience which has been gained in operating and reconstructing the tracks. This is partly because there are detector effects not included in the simulation such as the central inefficiency as demonstrated in section 6.1. This estimate should therefore be considered as the limit of uncertainty rather than a 1σ effect.

The systematic errors of the forward detector remain uninvestigated. One would expect that the simulation overestimates the efficiency of track finding as the simulated hits are generally of better quality than those actually observed. This is certainly the case in the central chamber as the variation of efficiency with pseudorapidity demonstrates.

4.2 Calorimeter Errors

The energy calibration of the calorimeters has been verified in DIS to be ±7% by studying the momentum balance between scattered electrons and the hadronic final state [29].

4.3 Cross section Measurement

The kinematical cuts for the cross section estimation were based on tracking information alone. In order to estimate the effects of lost and doubled tracks I ran the generator using MRSDO and LAC2 structure functions at a P_T^{min} cutoff of 2.0GeV with three track selections: 4% missing, 4% doubled; 0% missing, 8% doubled; and 8% missing, 0% doubled. From the spread in cross sections thus obtained I estimate a systematic error from kinematical cuts of +60%/-40%. The variations in tracks lost or gained affects cuts on both the scalar sum of transverse momenta, $\sum_{Tracks} P_t$, and the value of y_{track} as described in section 5.2.3.

The error from luminosity measurements is estimated to be about 7%. This was complicated in part by difficulties with the R.F. system which allowed the protons to become less bunched spreading out across 1m instead of the designed 0.5m. Thus the event vertices were more spread out. Detector acceptance is smaller for events occurring at the tails of this distribution which could cause an effective reduction in actual luminosity supplied to the experiment.

Uncertainties from the level 1 trigger efficiency are estimated to be around 4% as indicated in Chapter 5.

Thus the systematic uncertainty in the cross section measurement is dominated by uncertainties in the track reconstruction efficiency and, to 1 significant figure are +60%/-40%.

Chapter 5

Triggering and Data Aquisition(DAQ)

The challenge of selectively reducing a raw data volume of 3Mbytes arriving every 96ns to a final tape writing rate of 5Hz at a size of 120 Kbytes is answered by an adaptable modular system split into four stages. This allows each subdetector to run in independent mode for development and calibration whilst providing a standardised framework for combining and processing the total information.

5.1 The H1 Trigger

5.1.1 The Four Stage Trigger Scheme

As more refined information becomes available with each stage so sharper criteria for event rejection are applied. A 'pipeline' stores the raw information from the last $2\mu s$ in which the Level 1 logic decides whether or not to keep the event and start accumulating deadtime. Level 2 requires $20\mu s$ to improve the decision before actual digitisation starts. Level 3 further considers information whilst subdetector data is read out and reduced. If no reject signal is received the subdetectors are partially reconstructed by the 'Event Builder' and fed to the 4th level where sophisticated decisions based on 2-dimensional tracking and the topology of energy depositions are possible. The need for fast acting discerning trigger elements has greatly affected the H1 design.

During the period investigated the trigger levels 2 and 3 were not implemented. Severe problems were avoided as a problem with electron beam intensity limited the luminosity during this period.

5.1.2 The Level 1 Trigger

As raw data is collected it is stored in a memory 'pipeline' providing $2\mu s$ before a Level 1 trigger decision is required. Dead time starts if the event is accepted here. At this stage the rejection of spurious signals is paramount. Central to this process are the TOF counters which provide a rejection mechanism against particles produced in proton collisions entering the detector from outside of the beam pipe. At least one trigger element must provide a t_0. That is a fast signal, provided by MWPC's, the Central Tracker or in future the Liquid Argon Calorimeters, with enough resolution to uniquely identify the event with one bunch crossing.

Level 1 relies heavily on the fast acting proportional chambers. A particularly selective signal is provided by the forward and central MWPC's. These have pads which are read out to provide very rough space points along tracks. All combinations of the pads fired in an event are analyzed via reference tables to determine the possible origin in z and the results are entered into a histogram. The significance, S, of the peak bin containing P entries in relation to the average count in other bins, B, is determined using the formula,

$$S = \frac{P - B}{\sqrt{B}} \tag{5.1}$$

The lowest requirement to obtain a trigger from this is a significance of 1.5 or greater.

Another important trigger is the DC-RPIII trigger (Drift Chamber trigger using only radial and azimuthal coordinates). A subsample of the wires in CJC1 are used. These are read out at both ends but, before further processing, the collected charges are summed thus neglecting information concerning the z-coordinate. The configuration of wires in the central tracker ensures a high probability that a track will pass close to a sensitive wire such that small drift distances and hence fast response times are available. The axial projection is divided up into 13 segments. From the pattern of hit wires it is decided whether or not a particular segment

contains a track. Thereafter it is possible to select certain arrangements of segments to act as a trigger condition, for example back to back events. In this study I simply used the criterion that at least one segment had registered.

Photoproduction physics benefits from a very strong early signal provided by the electron tagger. This triggers on hits with an energy of more than 4GeV in the electron calorimeter of the luminosity system. Any hits in the photon detector or the Water-Cherenkov counter act as a veto causing a slight loss in efficiency. The geometrical arrangement of detectors, magnets and beam pipe result in an acceptance for this device as shown in Figure 5.1.

5.1.3 The Level 4 Trigger

None of the events satisfying the final cuts were rejected by the Level-4 trigger logic. Because the tag condition already provides a strong indication of interesting physics it is possible to have very loose criteria at this stage. After 'event building' on the farm, new information from the tracker provides the most powerful selection at this stage. Events were rejected if there were no tracks reconstructed whereas my final selection requires at least 4. Horizontal tracks, which indicate muons produced by background proton collisions before the detector, also caused events to be discarded. Finally the main vertex of tracks must be in the collision region.

5.1.4 Data Classification and Storage

At the reconstruction stage a module is run to identify the physics potential of remaining events. Simple physical variables are calculated, such as the total energy in the calorimeter or the identification of a muon in the iron, and used to flag the events as interesting for a particular line of analysis. An event may have more than one flag. All events are then written to Production Output Tapes (POTs) . Events with at least one positive flag are written to more compact archives called Data Storage Tapes (DSTs) after removing the large raw digitisation banks.

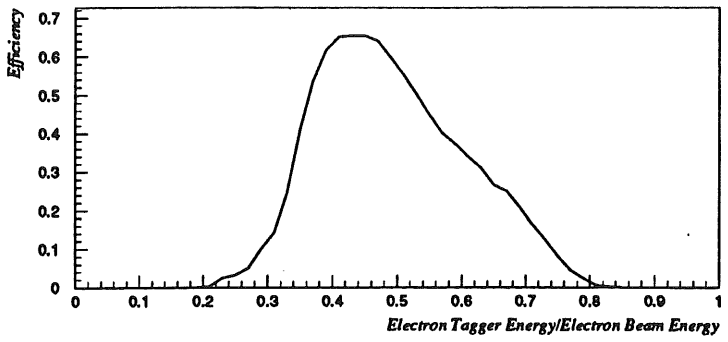

Figure 5.1: Electron Tagger Efficiency

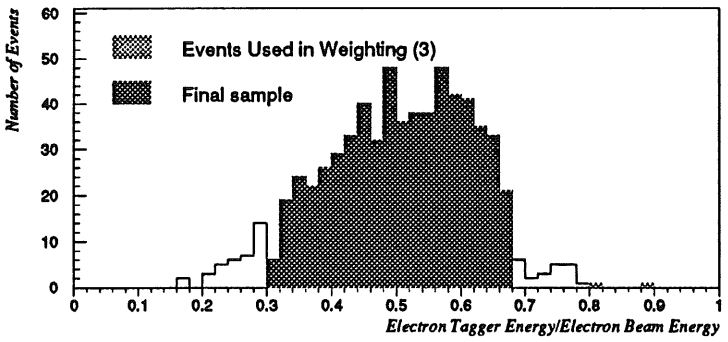

Figure 5.2: Electron Tagger Event Sample Distribution

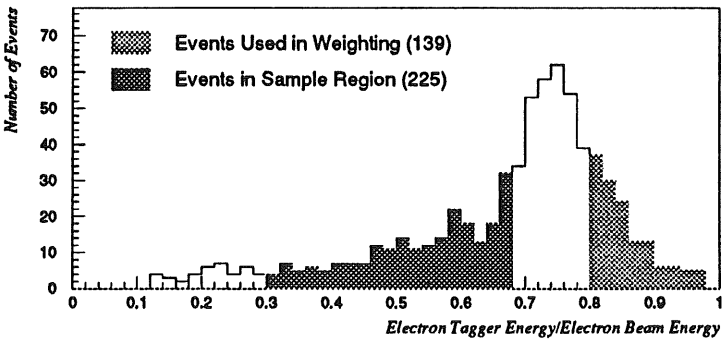

Figure 5.3: Electron Tagger Background Distribution

5.2 Event Selection

5.2.1 The level 1 Trigger

The events in my sample were triggered at level 1 by coincidence of electron tagger and one t_0 signal with TOF background rejection. Spurious signals from the electron tagger occur roughly once every 2000 events. These are entirely uncorrelated with background proton-gas and proton-beamwall collisions producing t_0 triggers. Hence there is an immediate reduction factor of 2000 against these background events.

The t_0 efficiency was monitored by using the electron tagger with TOF interaction signal. A sample using all the final cuts and selected by this trigger contained 162 events of which 158 were t_0 triggered. Thus the t_0 efficiency is roughly 97%±2%.

In a sample selected using the final event cuts with the Z-Vertex and DC-RPIII triggers there were 364 events. Of these 2 were vetoed by the photon tagger 16 by the water Cherenkov device and 7 by both whilst three events were vetoed by the TOF counter or veto walls. Thus an efficiency of 93%±1.5% for the photon-veto condition was established.

The main loss of signal originates from the electron tagger which has a geometrical acceptance determined by its size, shape and position as shown in Figure 5.1. This acceptance pattern was used as a cut in the Monte Carlo generated sample to allow direct comparison.

The acceptance and rejection peaks of the TOF overlapped slightly causing a loss of 3%±2%.

Thus the overall efficiency for the level 1 trigger excluding the electron tagger geometrical acceptance was 87.5%±4%.

5.2.2 Level 4

In my study, events with at least one vertex constrained track and an electron tagger trigger were used. These correspond to one of the event classes written in its entirety to DST. I expect no loss of signal at this stage as my final sample

Level 1 Trigger Efficiency		
Element	Efficiency %	Uncertainty %
Photon-Veto	93	1.5
T-Zero	97	2
TOF-Veto	97	2
Overall	87.5	4

Table 5.1: Level 1 trigger element efficiencies separate and combined

requires at least four vertex constrained tracks and a tag.

5.2.3 Kinematic Cuts

Further cuts are required to purge the remaining backgrounds. In order to sharply define the range of interacting photon energies, cuts were placed on the ratio of electron tagger and electron beam energies. Events were accepted if this ratio was greater than 0.3 and less than 0.68 (see Figure 5.2).

Central Tracker tracks were selected as detailed in Chapter 3 and used to select events as described below. Track information only was used in order to avoid triggering on spurious noise deposits in the calorimeter. Only tracks from the central region which can be reconstructed with high efficiency and good resolution are used. This measure allows cuts to be performed on the simulation before the full H1 reconstruction saving valuable computing resources and allowing a greater number of samples to be generated.

Cosmic rays are removed by requiring at least 2 positive and 2 negative tracks.

A powerful differentiator is the y_{track} parameter calculated as:

$$y_{track} = \sum_{tracks} \left(\frac{E - P_z}{2} \right) \tag{5.2}$$

This quantity theoretically reproduces the energy of the object struck by the proton. In the case of background from struck nucleons this is limited to approximately 1GeV, whilst for photoproduction it is the momentum of the photon or parton from the photon in the hard process. Although these are the theoretical maxima, the

acceptance cuts imposed on tracks reduces the observed value considerably. A cut of 2GeV was placed on this parameter.

The quantity $\sum_{Tracks} P_t$ is calculated by summing the magnitude of transverse momenta of all tracks selected. Events with less than 5.5GeV/c in this quantity were removed. This was done to reject backgrounds, to eliminate the soft-scatter components of the cross-section and to reach a regime of high acceptance of the cut in y_{track} (Figure 5.4) As a guide, the RAYVDM Monte Carlo (a combination of RAYPHOTON [30] to generate the photon flux and LUCVDM [31] to model the subsequent interaction) was used as shown in Figure 5.5 after implementation of the y_{track} cut.

A cut was placed on the event vertex between ±44cm in z from the nominal interaction point (Figure 5.7).

5.2.4 Checks of background Contamination

The electron tagger provides a powerful indication of the remaining background in the event sample. The tagger has an acceptance for electrons originating from photoproduction physics which falls to zero when the scattered electron has greater than four fifths of the electron beam energy (Figure 5.1). Above this value the events are purely background. The energy spectrum for background is fully independent of the cuts imposed on tracks and clusters, since it arises through a random coincidence of beam-wall or beam-gas collision generating a I_0 element and a false signal from the electron tagger. During the runs one bunch was operated without protons. By scaling this background energy spectrum shown in Figure 5.3 to match the number of events seen in the region of zero acceptance an accurate estimate of the remaining incidentals can be calculated. In the background sample there are 139 events in the region of zero tagger efficiency and 225 events in the sensitive region. In the zero efficiency region of the physics sample (Figure 5.2) only 3 events were found suggesting contamination at the level of about 6 events or 1%. This was ignored in further analysis.

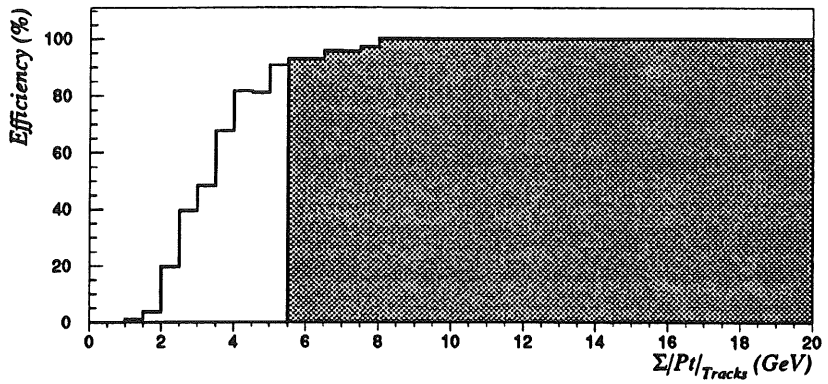

Figure 5.4: Acceptance of y_{track} cut

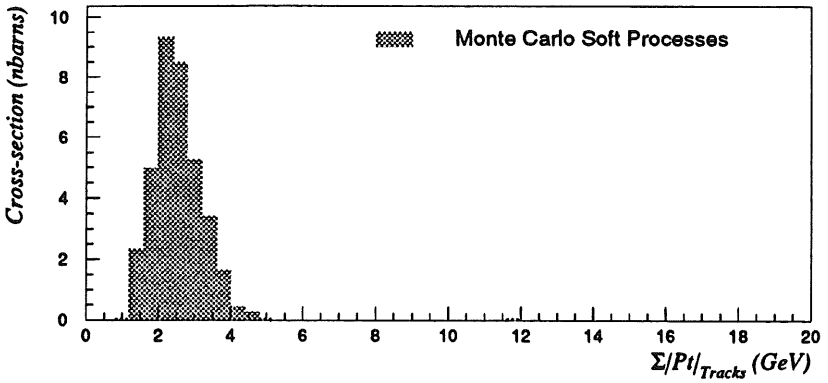

Figure 5.5: Background from non-perturbative interactions

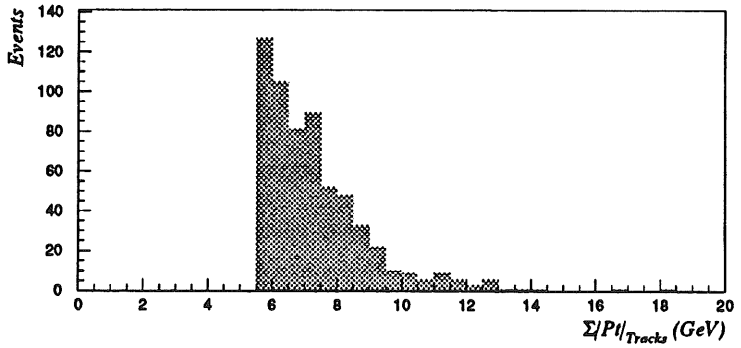

Figure 5.6: Distribution of accepted data events

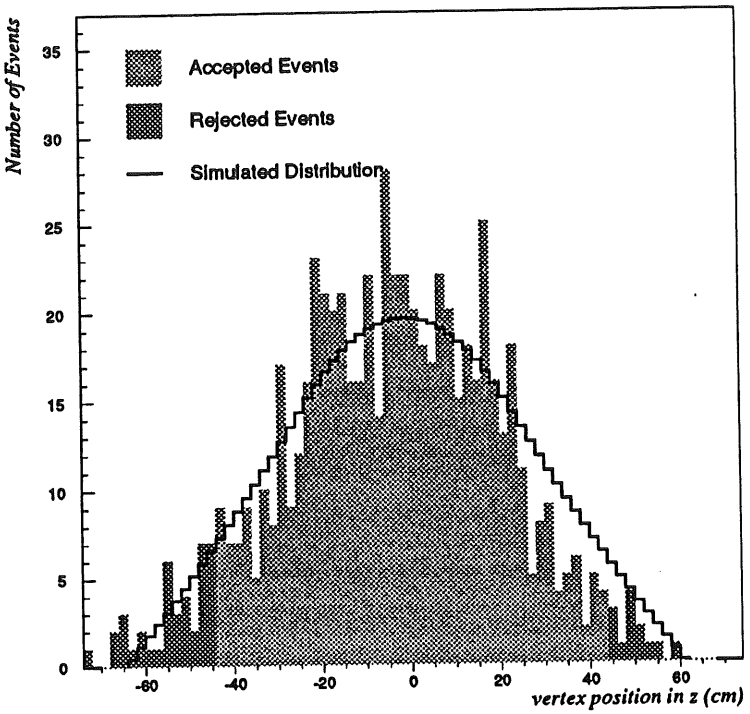

Figure 5.7: Distribution of event vertices in z

5.3 Cross-section Measurement

The number, N, of events which survived all cuts was 611. Hence, using the equation,

$$\sigma = \frac{N}{\mathcal{L}\varepsilon} \tag{5.3}$$

for an integrated luminosity , $\mathcal{L}$, of 24.9nb^{-1} and efficiency, ε, of 87.5%, one calculates a cross-section in electron-proton collisions, σ, for selected events of 28nb with 1nb statistical error .

This is compared in Figure 5.8 with two choices of structure function across a range of P_T^{min}. The points indicated correspond to full Monte Carlo detector simulation and reconstruction with statistical errors. Due to the effects of weighting the errors are much larger on the points with lower P_T^{min}. The lines drawn through these points were constructed from simulation at the generator level and then reweighted to coincide with the more accurate reconstruction. Level 1 triggers, other than the geometrical acceptance of the electron tagger, were not reconstructed in the simulated samples so here the efficiency, ε, is 1. Cuts were placed on

the 4-vectors at the generator level in order to avoid simulating and reconstructing many events which had no chance of being finally accepted. Only charged particles between 28 and 152 degrees were used with cuts on y_{track} and $\sum_{tracks} P_T$ at 1.0 and 2.5GeV/c respectively. These cuts were looser than those after full reconstruction such that events with doubled tracks or poor measurements would not be excluded prematurely.

There is clearly a strong dependance between the structure functions used and the required P_T^{min}. The two sets used were considered to be limiting cases of gluon structure function tending to a constant (MRSD0,LAC2) or rising sharply (MRSD-,LAC1a). Within these limits and despite large systematic uncertainties a P_T^{min} value between 2.0 and 3.0GeV/c is preferred. This is consistent with preliminary measurements of the total photon-proton cross section from HERA [10, 11]. Presently, the HERA data supports a proton structure function with a sharp increase in the low-x region as described by MRSD-. As this is better measured and the understanding of systematics of detectors is improved it should be possible to constrain more tightly the photon structure function and cutoff parameter.

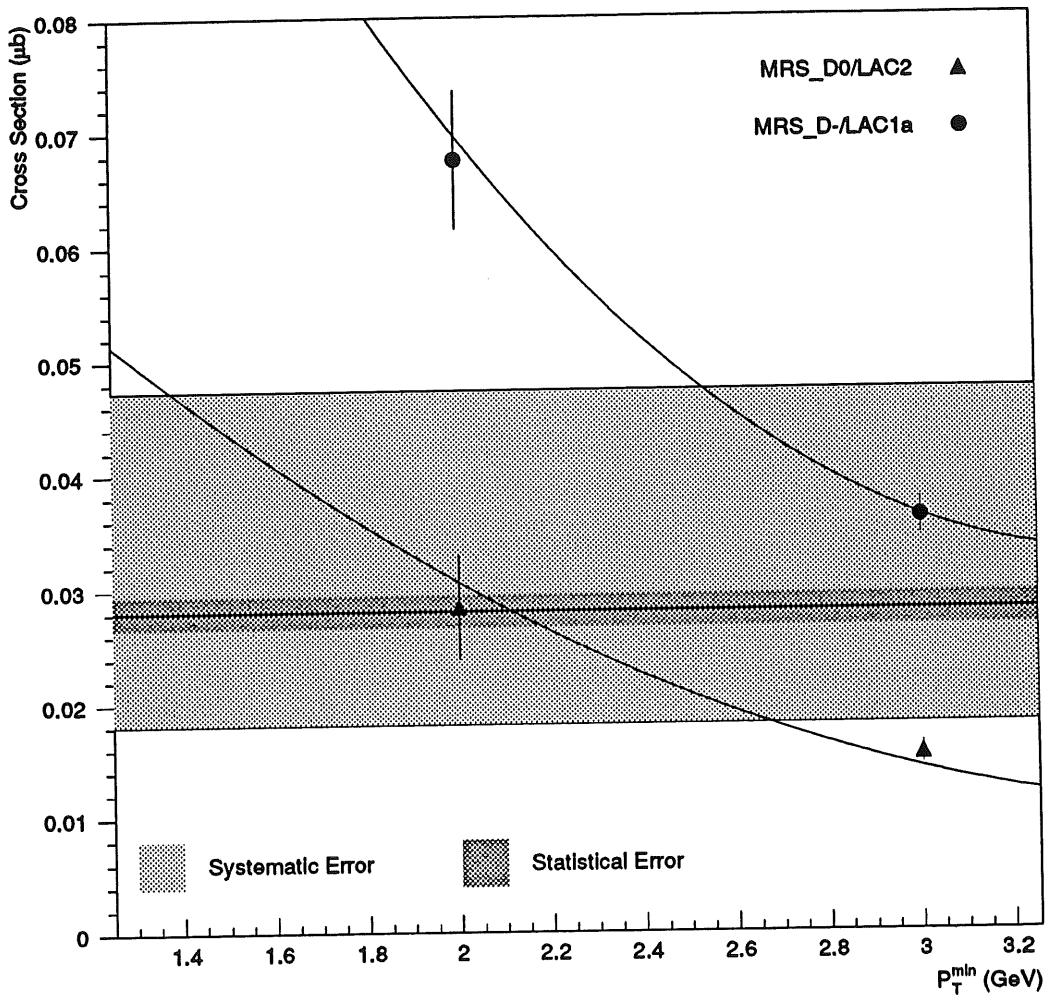

Figure 5.8: Cross-Section Measurement and Predictions

Chapter 6

Inclusive Distributions of Charged Particles

I have divided each histogram in this section by the number of events in the sample thus rendering the normalization independent of cross section differences between simulation and data. These tracks are selected as described in chapter 3. The simulation used for comparison has been generated using the MRS_D0 and LAC2 structure functions with P_T^{MIN} values of 2 and 3GeV/c.

6.1 Central Tracks

Figure 6.1 shows the distribution of transverse momentum squared for the central region. The shaded histogram is derived from simulation of hard subprocesses whilst the cross bars are data points with associated statistical errors. Systematic errors, expected to be no greater than 8%, as described in section 4.1, are not shown. The agreement is very good although there is a deficit of tracks in the lowest bins. At first the distribution falls off very steeply decreasing at an exponential of perhaps 5 or 6 times the transverse momentum squared. The higher energy region is characterized by a much slower decline. This pattern is characteristic of QCD scattering processes [28].

Shown in Figure 6.3 and Figure 6.2 are the inclusive pseudorapidities in the lab frame of charged tracks with transverse momentum squared greater than and

less than 3GeV^2 respectively. The prediction from simulation is denoted by the shaded areas and is split into direct and resolved contributions. The resolved part is further subdivided according to the combination of initial partons colliding; gluon-gluon, gluon-quark or quark-quark. The simulated distributions have been smoothed using splines in order to make the graphs simpler to read.

Although the overall number of tracks is similar, the shape of the distribution shows some marked differences from the simulated prediction. Most noticeably there is a dip in the central region. This probably arises from the variation of pulse height with track crossing angle. The length of track, L, contributing to the pulse on a particular wire is a function of the wire separation, l, and the polar angle of the track:

$$L = \frac{l}{\sin\theta} \tag{6.1}$$

Hence pulses produced by tracks in the middle of the chamber are smaller than those at the edges. Pulse size differences also arise due to variations in particle type and momentum. The signal amplification electronics must be carefully adjusted in order to maintain accuracy for the wide range of pulses recorded. Hopefully this situation can be improved in future operation. The H1 simulation program does not produce pulse shapes for analysis but rather generates a set of hits distributed on wires with typical spread determined by resolution.

In Figure 6.2 there is a gradual rise with increasing pseudorapidity which appears also to be the general trend in the data. The scatter of data points in Figure 6.3 makes comparison with simulation more difficult.

It is clear that the direct part provides only a small fraction of events. Its contribution is smaller than the statistical spread of data points. The dominating processes are gluon-gluon or gluon-quark scattering demonstrating the importance of gluon structure functions in these processes. One should note that the distributions are of roughly similar shape eliminating the possibility of any study of relative subprocess contributions.

The 'hard' simulation seems capable of explaining the complete spectrum. Thus there is no need for the soft contribution after the cuts have been applied.

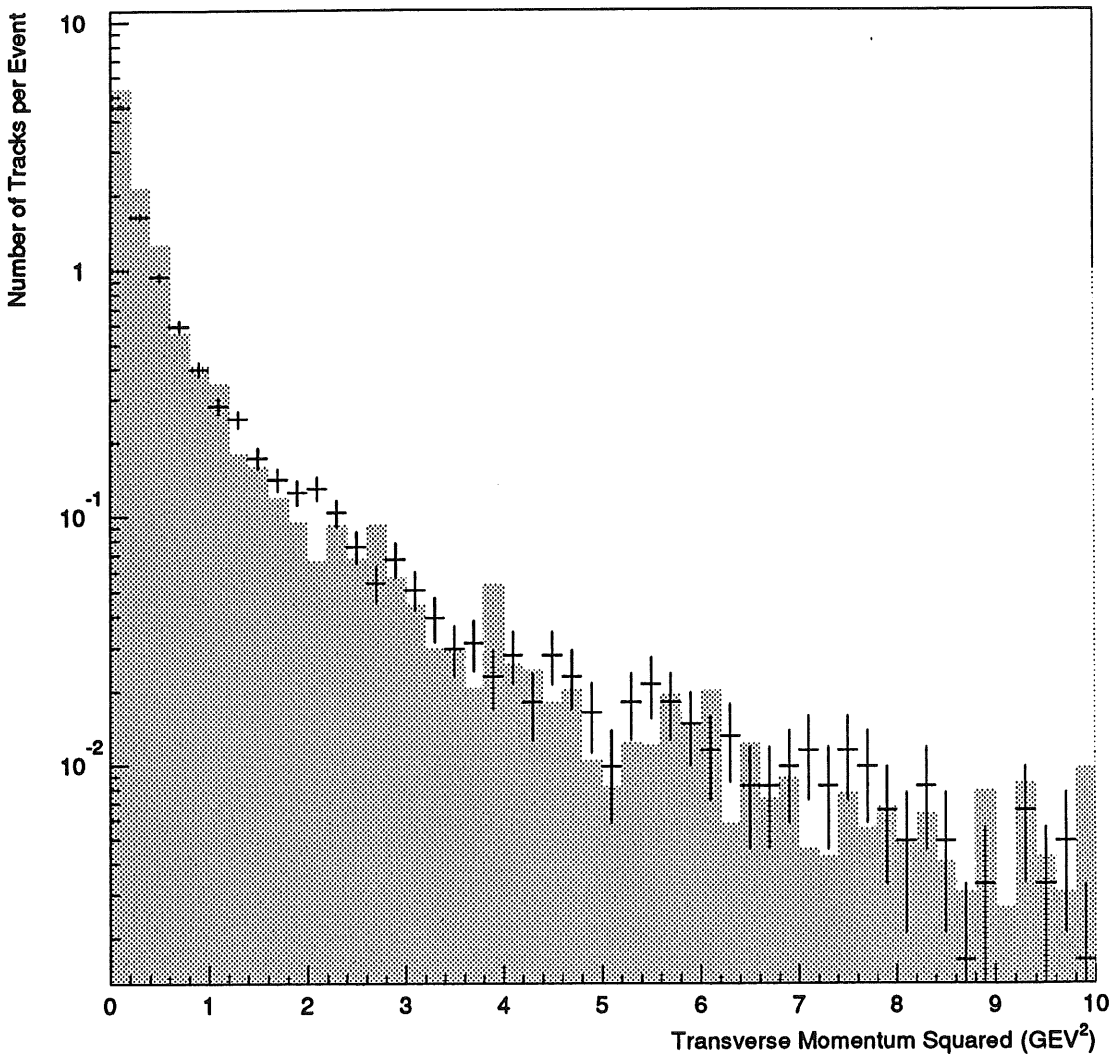

Figure 6.1: Inclusive Distribution of Squared Transverse Momentum of Central Charged Tracks

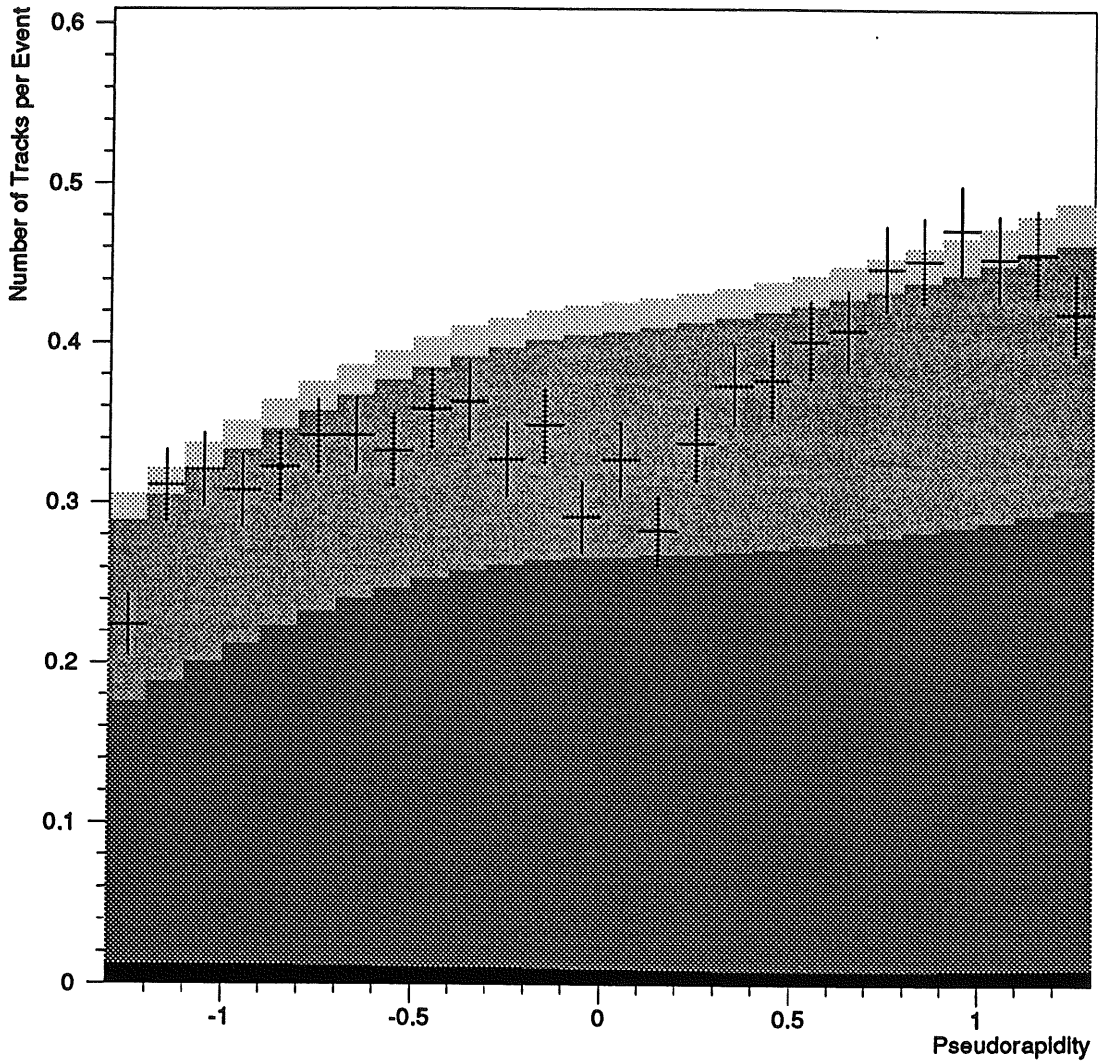

Figure 6.2: Inclusive Distribution of the Pseudorapidity of Central Charged Tracks: Squared Transverse Momentum Less Than $3GeV^2$

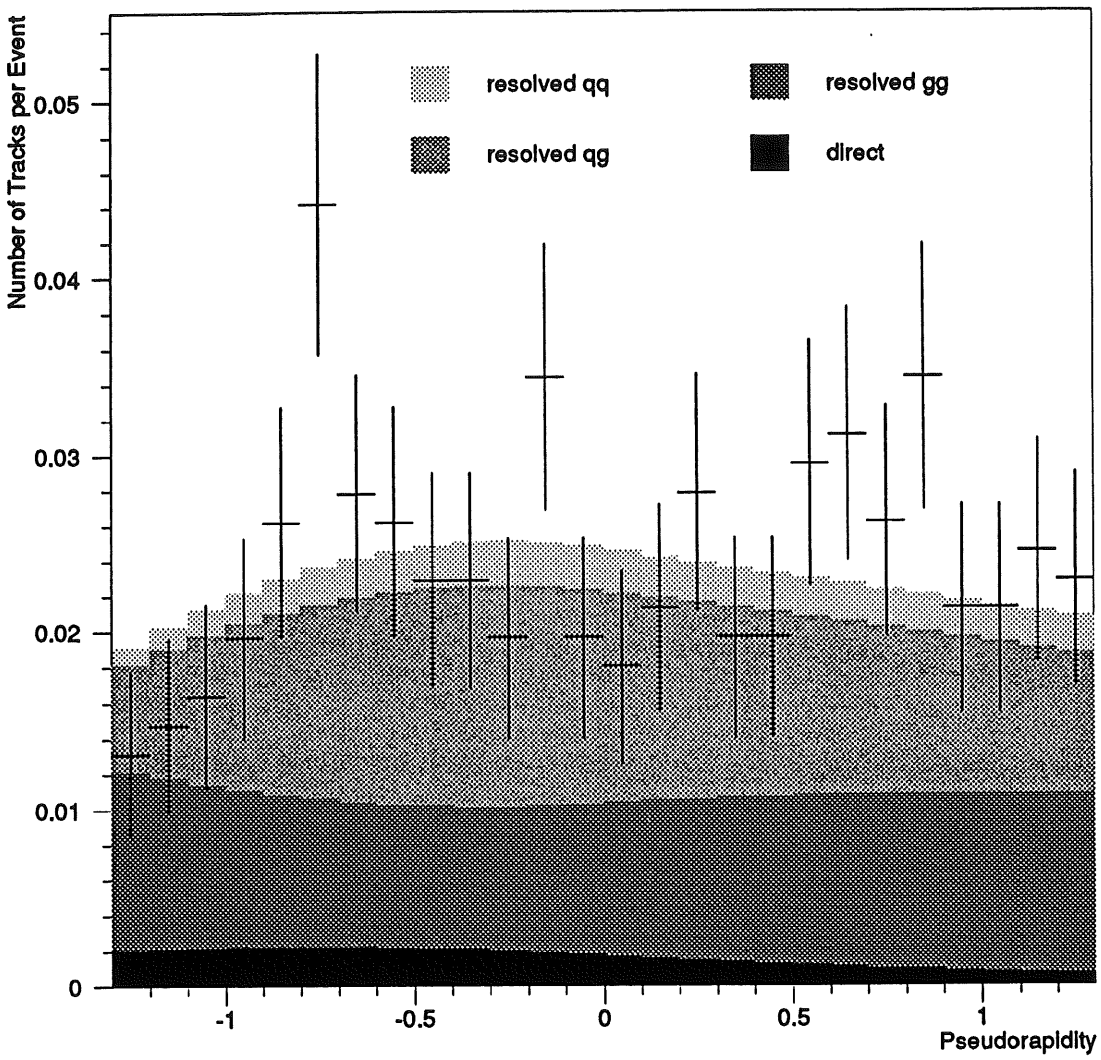

Figure 6.3: Inclusive Distribution of the Pseudorapidity of Central Charged Tracks: Squared Transverse Momentum Greater Than 3GeV^2

6.2 Forward Tracks

The inclusive distributions of transverse momentum squared and pseudorapidity for charged tracks in the forward tracker are shown in Figure 6.4 and Figure 6.5 respectively.

Once again the squared transverse momentum shows close agreement with simulation. The high energy tail of this distribution has been rebinned to retain statistical accuracy.

The pseudorapidity distribution, whilst generally having the same number of tracks per event, shows a marked difference in shape with a definite excess of data between pseudorapidity values of 1.6 and 2.3.

The data and simulation show reasonable consistency given all the imperfections in the forward tracker at this early stage in the life of the experiment.

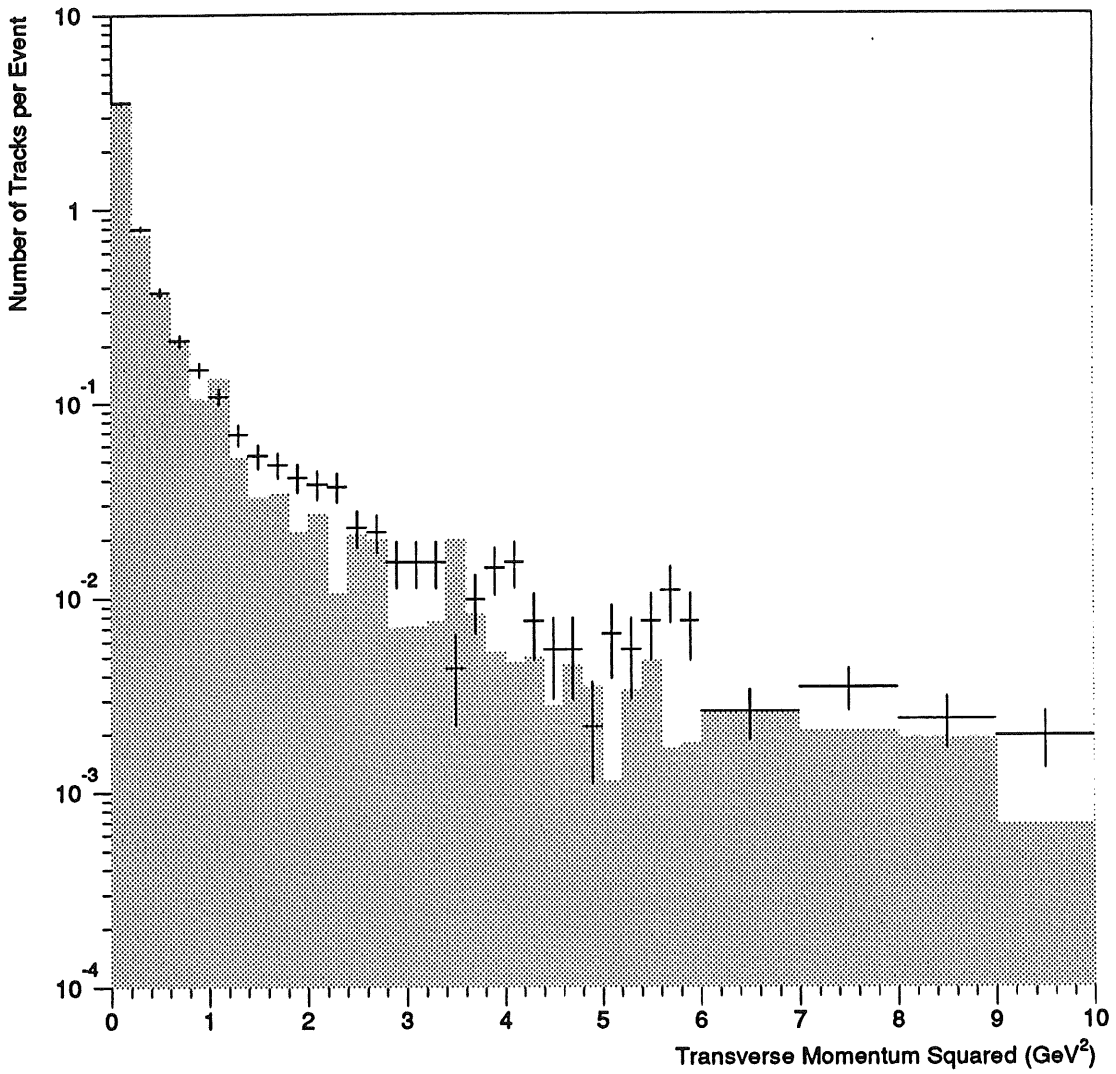

Figure 6.4: Inclusive Distribution of Squared Transverse Momentum of Forward Charged Tracks

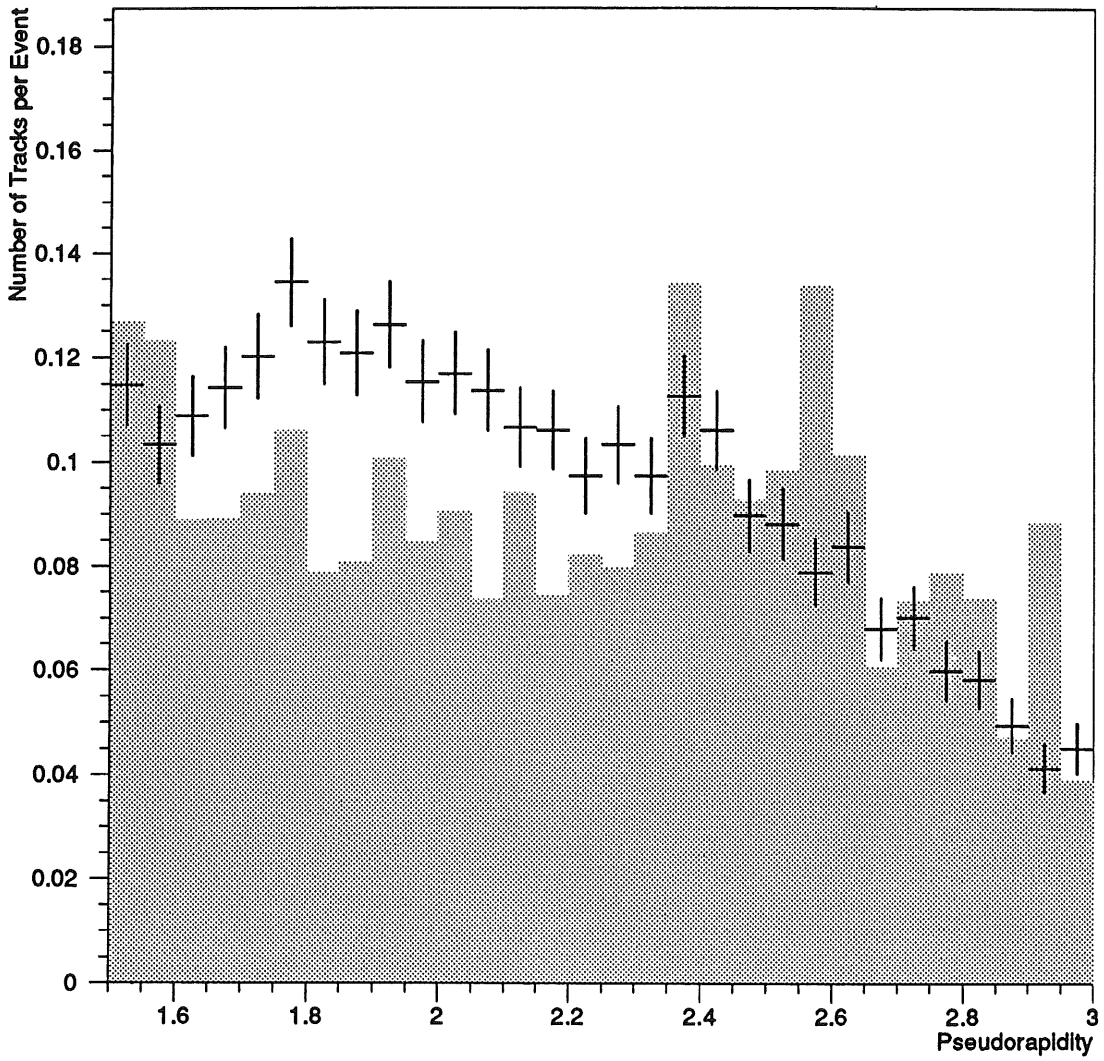

Figure 6.5: Inclusive Distribution of the Pseudorapidity of Forward Charged Tracks

Chapter 7

Analysis of Energy Flow

7.1 Combining Tracks and Clusters

I have attempted three different methods of reconstructing the energy flow. In any event the most accurate measurement of energy flow can be derived from the tracking. This doesn't give a complete picture as all neutral particles are unrecorded causing a loss of signal, the size of which fluctuates from event to event. A less precise but in principle more complete picture of energy flow can be derived from the calorimeter. Here the main source of fluctuation comes from statistical development of electromagnetic and hadronic showers in the calorimeter stacks. Probably the best solution is to use some combination of tracks and clusters in order to obtain the best resolution. This is not a simple job as some scheme must be implemented to avoid 'double counting', that is adding in the contribution of a charged particle from both its track and cluster.

7.1.1 Clusters Only

The simplest method is to ignore tracks and just use the calorimeter, thus avoiding all problems of incomplete information and double counting but foregoing the resolution of the tracker. The non-compensating calorimeter causes some difficulties as different conversion scales must be used for electromagnetic and hadronic showers. Identification can be done by looking at the shape and size of showers but some confusion is inevitable and the algorithms used were not developed for

the very low energy deposits being considered here.

7.1.2 Tracks and Unmasked Electromagnetic Clusters

The majority of energy flow is carried by pions. The charged pions generally leave a charged track and deposit energy in the hadronic calorimeter. The neutral pions generally decay into two gammas which leave no trace in the tracker and deposit energy in the electromagnetic calorimeter. Thus a scheme may be devised where the tracks are used to account for charged pions and electromagnetic clusters are used for the neutral pions. The information in the hadronic calorimeter is ignored. Electromagnetic clusters found in the region where a track intercepts the calorimeter are also excluded to avoid cases where charged pions deposited energy in the electromagnetic calorimeter.

7.1.3 Weighted Sum of Tracks and Clusters

One way to sidestep some of the problems mentioned above is to identify the hadronic energy deposition using the tracker and use this to decide which energy scale to use when converting charge deposition into equivalent energy. This also avoids the risk of double-counting and loss of masked cells found in the above method for combining tracks and clusters.

Assume that there is a total charge deposited in the calorimeter which, when converted to the electromagnetic scale, is equivalent to an energy, ϵ. Some fraction, λ, of this energy originates from hadrons, E_{had}, whilst the remaining fraction, $(1-\lambda)$, is electromagnetic, $E_{e/m}$. The hadronic fraction must be multiplied by a factor of 1.5 to be correctly reconstructed. Thus we have:

$$E_{e/m} = (1-\lambda)\epsilon \tag{7.1}$$

$$E_{had} = 1.5\lambda\epsilon \tag{7.2}$$

Assuming a high efficiency for track reconstruction and neglecting neutral hadrons one could argue that:

$$E_{had} = E_{track} \tag{7.3}$$

Rearranging gives

$$\lambda = \frac{E_{track}}{1.5\epsilon} \tag{7.4}$$

and

$$E_{\epsilon/m} = \epsilon - \left(\frac{E_{track}}{1.5}\right) \tag{7.5}$$

The total energy, E_{tot}, is simply the sum of electromagnetic and hadronic which quickly leads to the conclusion

$$E_{tot} = \epsilon + \frac{E_{track}}{3} \tag{7.6}$$

This could be thought of simply as the correct treatment of electromagnetic energy plus the hadronic energy at the electromagnetic scale with a correction supplied by the tracks.

7.1.4 Evaluation of Reconstruction Schemes

The three schemes have been tested by comparing the fully reconstructed Monte-Carlo simulation with the momenta of particles emerging from the event generator. For each case, the generated particles have been selected using criteria designed to match those in the particular scheme. The cluster only scheme was compared to any particles with greater than 0.6GeV/c transverse momentum. The tracks and unmasked electromagnetic clusters were compared to charged particles with more than 0.1GeV/c and photons with more than 0.6GeV/c transverse momentum. For the weighted sum of tracks and clusters the comparison was with charged particles cut at 0.1GeV/c weighted by a third, plus charged and neutral hadrons cut at 0.6GeV/c weighted by two thirds, plus leptons with more than 0.6GeV/c. The difference between the scalar sum of transverse momenta for each scheme and the corresponding transverse momenta from the event record of generated particles are given. These are divided into four ranges in the transverse momenta as measured using the generated particles (Figure 7.1). Each bar is centered on the average difference of reconstructed and generated energies and extends either side a distance equal to the root mean square spread of this distribution.

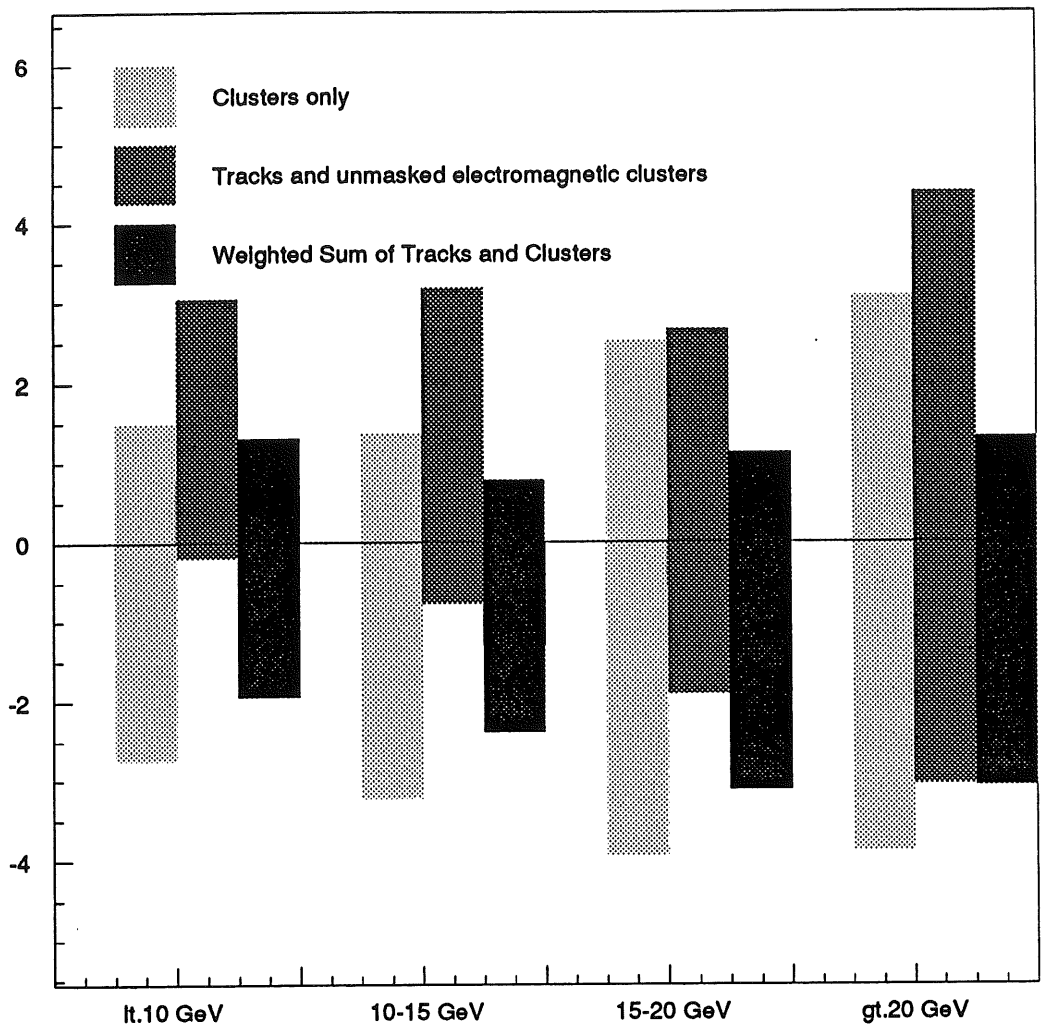

Figure 7.1: Reconstructed minus generated transverse momenta for three reconstruction schemes.

Whilst it is clearly possible to improve on the measurement of clusters by adding information from the tracker, none of the schemes produce a startling improvement. The weighted sum of tracks and clusters seems the best scheme at the highest energy range.

7.2 Distributions of Clusters

7.2.1 The Cluster Algorithm

I decided to use a cone algorithm since it would be simple to understand and operate. A grid was constructed to cover the region of the central tracker with 24 azimuthal divisions and 26 pseudorapidity divisions between +/- 1.3. Firstly the transverse momenta of all the selected tracks and clusters falling within these bins were summed. Bins with resulting transverse momentum greater than 1GeV/c were considered as possible initiators and treated in falling order of deposited momentum. All bins falling within a radius of 1 in units of radians and pseudorapidity were summed and those with transverse momentum sum greater than a predetermined minimum cutoff were accepted as clusters. These selected bins were then removed from further analysis and the process repeated until all the possibilities were exhausted.

7.2.2 Evolution of Number of Reconstructed Clusters

In this study the selection of tracks and unmasked electromagnetic clusters has been used throughout. For each event I have run the cluster algorithm five times with minimum cluster momentum acceptance cuts ranging from 3 to 7 GeV/c. This is designed to show transition from the regions dominated by fragmentation effects to those where partonic event structure is starting to emerge. To order the results I have histogrammed separately those events with 0,1 or 2 clusters accepted. Very few events had more than 2 clusters. Each histogram (Figures 7.2 - 7.4) shows the event distribution as a function of minimum cluster momentum acceptance with each bin divided by the total sample size. I have further divided the sample into those events in which the total transverse momentum was between 10 and 15GeV/c, between 15 and 20GeV/c or greater than 20GeV/c. As the minimum cluster transverse momentum cut is increased the number of events in which no clusters are found rises whilst those with two clusters found falls.

The data and simulation produce similarly shaped distributions throughout. Those events with greater than 20GeV/c are least well reproduced. There is a

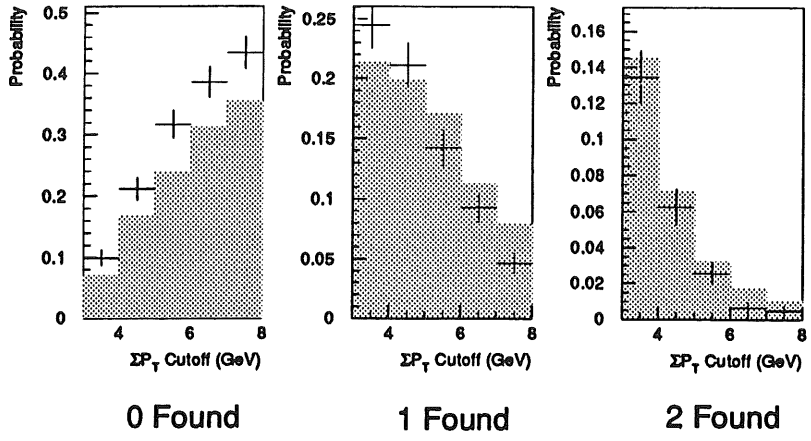

Figure 7.2: Energy Cluster Distributions $\sum P_T$ 10-15GeV/c

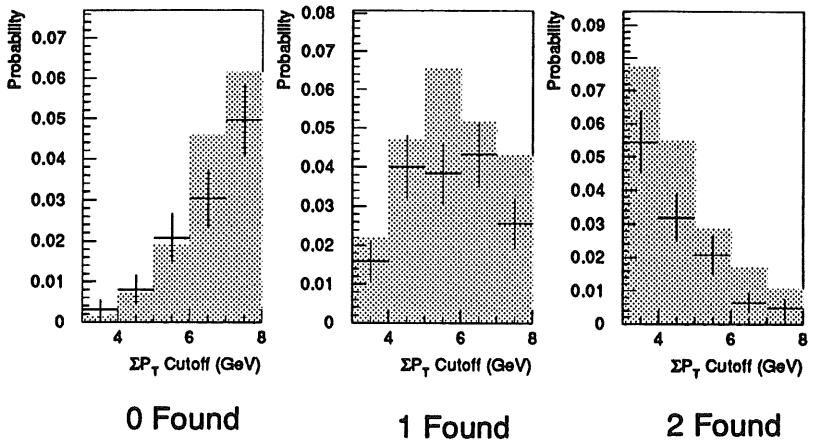

Figure 7.3: Energy Cluster Distributions $\sum P_T$ 15-20GeV/c

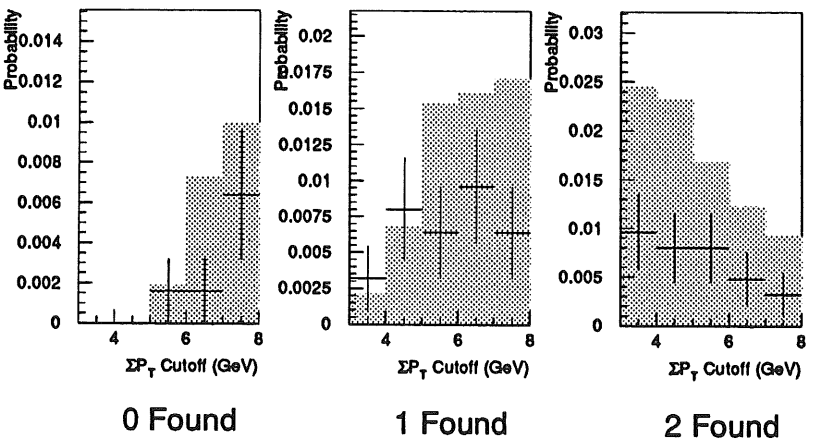

Figure 7.4: Energy Cluster Distributions $\sum P_T$ over 20GeV/c

deficiency in the overall number of these events and too many events between 10 and 15GeV/c without any clusters reconstructed. Nevertheless the data is on the whole well represented by the 'hard' simulation prediction.

7.3 Resultant Transverse Momentum

This distribution is included to study the effect of initial state radiation. This mechanism refers to the multiple radiation of partons from the interacting parton prior to the hard process. Each radiation reduces the x value of the parton but increases its transverse momentum leading to a considerable net transverse momentum of the final state.

In Figures 7.5 and 7.6 I have plotted the normalized resultant transverse momentum distribution of the central region. This has been done for the two selection schemes: tracks and unmasked electromagnetic clusters in Figure 7.5 and the weighted sum of tracks and clusters in Figure 7.6. In each case the data is represented by cross bars with verticals indicating the statistical errors. Simulations with initial state radiation, indicated by the shaded histogram, and without initial state radiation, indicated by the hatched histogram are also drawn.

Within the limits of statistical errors there seems general agreement between the data and simulation distributions. No significant difference is observed between the simulations with and without initial state radiation. Many mechanisms can destroy the effect produced by initial state radiation including poor detector resolution and bias introduced by cuts. The prediction is for many events to consist of one parton moving into the forward region with one remaining in the centre leading to large resultant transverse momenta in the measured region.

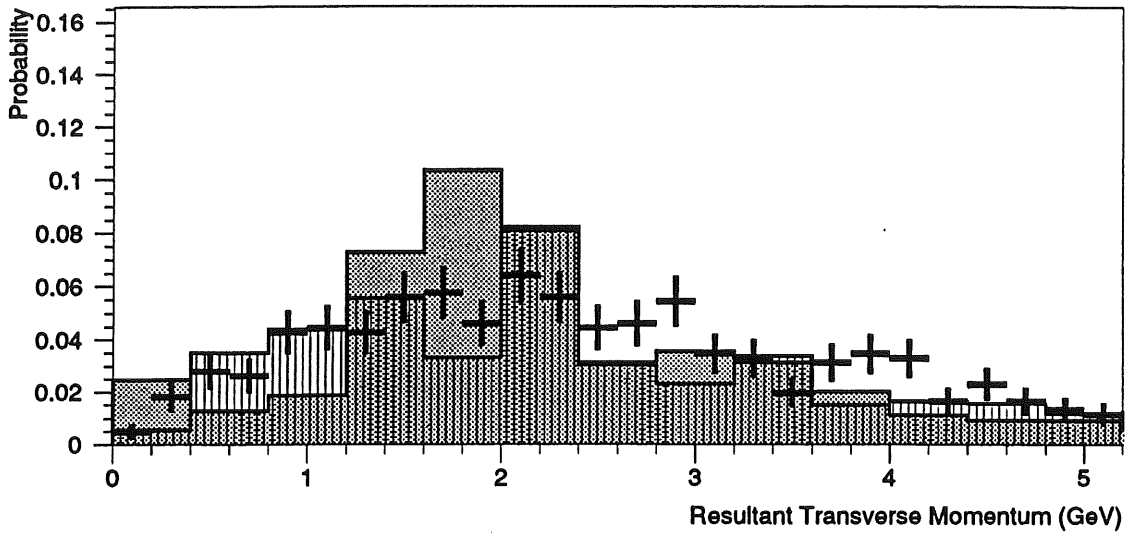

Figure 7.5: Resultant Transverse Momentum: Tracks and Unmasked Electromagnetic Clusters

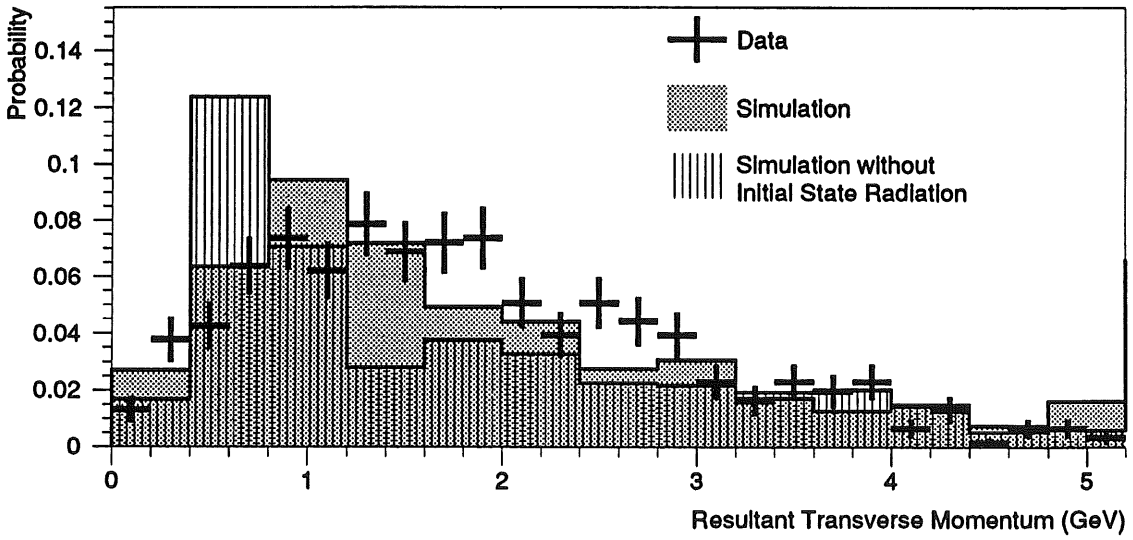

Figure 7.6: Resultant Transverse Momentum: Weighted Sum of Tracks and Clusters

Chapter 8

Conclusions

In this thesis I have studied a sample of 611 events selected using tagged electrons and kinematical cuts based on charged tracks. These were recorded by the H1 Collaboration in the August to October period of the first year of data collection, 1992, at the HERA electron-proton collider. The cross section has been compared with 'hard' QCD 2 body scattering models produced by the generator PYTHIA version 5.6 passed through complete detector simulation and reconstruction packages. Two sets of structure functions have been considered across a range of values for the P_T^{min} cutoff parameter.

In this analysis a new threshold has been crossed between HERA and previous experiments allowing a previously inaccessable region of high momentum transfer processes to be investigated. The models of photon-proton interaction previously developed have been entirely adequate to describe the data recorded in this region.

8.1 Cross Section Measurement

The cross section for the events selected has been shown to be consistent with either: MRSD0 proton and LAC2 photon structure functions for a P_T^{min} cutoff parameter of 2GeV/c, or; MRSD- proton and LAC1a photon structure functions for a P_T^{min} cutoff parameter of about 3GeV/c or greater. These results are consistent with earlier measurements from HERA of the total photon-proton cross section [10, 11] and also a previous study by H1 where kinematical cuts were based on

calorimeter measurements [33]. A recent study from the ALEPH collaboration at LEP has also favoured a cutoff parameter in this range [9]. Although earlier results from AMY [7] and TOPAZ [8] have favoured lower values, these studies were conducted at lower energies and used samples dominated by low momentum transfer events.

The first measurements of proton structure function from HERA [32] have favoured an evolution at low-x values which matches closely the MRSD- description. As this variable becomes more precisely determined and the understanding of detector systematic errors improves it will be possible to place tighter constraints on the photon structure function and QCD-cutoff parameter P_T^{min}.

8.2 Investigation of Inclusive Track Distributions and Energy Flow

A study of inclusive track distributions has shown close agreement with the simulation. In particular the distribution of squared transverse momentum shows the normal characteristics of such events. Uncertainties are still dominated by poor understanding of detector response. Simulated distributions of pseudorapidities show that direct processes account for less than 10% of the sample which is dominated by interactions involving gluons.

Different mechanisms for reconstructing the energy flow were compared and the advantages of combining information from both tracking and calorimetry was demonstrated. A cone algorithm was used to investigate the evolution of clustering with transverse momentum of the event and close agreement between data and simulation was observed. Plots of the resultant transverse momentum also showed no discrepancy.

The data was found to be consistent with the simulated 'hard process' simulation lending weight to the claim that the event sample is largely free of the low momentum transfer events that have previously dominated photon interaction studies.

Appendix A

QCD Cross-Sections

For the 2 body scattering processes used in this study I list the appropriate Feynman Diagrams, matrix elements and cross-section formlae [34].

A.1 Resolved Processes

$$\frac{d\sigma_{res}\left(ep \rightarrow jj\right)}{d\,p_T} = 2\,p_T \int_{y^{min}}^{1} dy \int_{x_p\ ^{min}}^{1} d\,x_p\ f_{\gamma/e}\left(y, E^2\right) \int_{x_\gamma\ ^{min}}^{1} d\,x_\gamma\ \frac{1}{1+\delta_{cd}}$$

$$\sum_{a,b} q_a^P\left(x_p\,,\,Q^2\right) q_b^\gamma\left(x_\gamma\,,\,Q^2\right) \left[\frac{d\hat{\sigma}\left(ab \rightarrow cd\right)}{d\hat{p}_T^2}\left(\hat{s}\,,\,\hat{t}\,,\,\hat{u}\right) + \frac{d\hat{\sigma}\left(ab \rightarrow cd\right)}{d\hat{p}_T^2}\left(\hat{s}\,,\,\hat{u}\,,\,\hat{t}\right)\right]$$

$$y^{min} = \frac{4\ {p_T}^2}{s}$$

$$x_p\ ^{min} = \frac{4\ {p_T}^2}{ys}$$

$$x_\gamma\ ^{min} = \frac{4\ {p_T}^2}{yx_P s}$$

$$\left|\overline{M}\left(qq\prime \rightarrow qq\prime\right)\right|^2 = \left|\overline{M}\left(q\bar{q}\prime \rightarrow q\bar{q}\prime\right)\right|^2 = \frac{64\pi^2\alpha_s^2}{9}\left(\frac{\hat{s}^2\ +\ \hat{u}^2}{\hat{t}^2}\right)$$

$$\left|\overline{M}\left(qq \rightarrow qq\right)\right|^2 = \frac{64\pi^2\alpha_s^2}{9}\left(\frac{\hat{s}^2\ +\ \hat{u}^2}{\hat{t}^2} + \frac{\hat{s}^2\ +\ \hat{t}^2}{\hat{u}^2} - \frac{2}{3}\frac{\hat{s}^2}{\hat{t}\hat{u}}\right)$$

$$\left|\overline{M}\left(q\overline{q}\rightarrow q'\overline{q}'\right)\right|^2 = \frac{64\pi^2\alpha_s^2}{9}\left(\frac{\hat{t}^2+\hat{u}^2}{\hat{s}^2}\right)$$

$$\left|\overline{M}\left(q\overline{q}\rightarrow q\overline{q}\right)\right|^2 = \frac{64\pi^2\alpha_s^2}{9}\left(\frac{\hat{s}^2+\hat{u}^2}{\hat{t}^2}+\frac{\hat{t}^2+\hat{u}^2}{\hat{s}^2}-\frac{2}{3}\frac{\hat{u}^2}{\hat{s}\hat{t}}\right)$$

$$\left|\overline{M}\left(q\overline{q}\rightarrow gg\right)\right|^2 = \frac{128\pi^2\alpha_s^2}{3}\left(\frac{4}{9}\frac{\hat{t}^2+\hat{u}^2}{\hat{t}\hat{u}}-\frac{\hat{t}^2+\hat{u}^2}{\hat{s}^2}\right)$$

$$\left|\overline{M}\left(qg\rightarrow qg\right)\right|^2 = 16\pi^2\alpha_s^2\left(\frac{\hat{s}^2+\hat{u}^2}{\hat{t}^2}-\frac{4}{9}\frac{\hat{s}^2+\hat{u}^2}{\hat{s}\hat{u}}\right)$$

$$\left|\overline{M}\left(gg\rightarrow q\overline{q}\right)\right|^2 = \frac{8\pi^2\alpha_s^2}{3}\left(\frac{1}{3}\frac{\hat{t}^2+\hat{u}^2}{\hat{t}\hat{u}}-\frac{3}{4}\frac{\hat{t}^2+\hat{u}^2}{\hat{s}^2}\right)$$

$$\left|\overline{M}\left(gg\rightarrow gg\right)\right|^2 = 72\pi^2\alpha_s^2\left(3-\frac{\hat{t}\hat{u}}{\hat{s}^2}-\frac{\hat{s}\hat{u}}{\hat{t}^2}-\frac{\hat{s}\hat{t}}{\hat{u}^2}\right)$$

$$\frac{d\hat{\sigma}}{d\,{p_T}^2} = \frac{\left|\overline{M}\right|^2}{16\pi\,\hat{s}\left(\hat{s}+2\,\hat{t}\right)}$$

A.2 Direct Processes

$$\frac{d\sigma_{dir}\left(\epsilon p\rightarrow jj\right)}{d\,p_T} = 2\,p_T\int_{y^{min}}^{1} dy\int_{{x_p}^{min}}^{1} d\,x_p\; f_{\gamma/\epsilon}\left(y,E^2\right)$$

$$\sum_a q_a^P\left(x_p,Q^2\right)\left[\frac{d\hat{\sigma}\left(\gamma a\rightarrow cd\right)}{d\hat{p}_T^2}\left(\hat{s},\hat{t},\hat{u}\right)+\frac{d\hat{\sigma}\left(\gamma a\rightarrow cd\right)}{d\hat{p}_T^2}\left(\hat{s},\hat{u},\hat{t}\right)\right]$$

$$y^{min} = \frac{4\;{p_T}^2}{s}$$

$${x_p}^{min} = \frac{4\;{p_T}^2}{ys}$$

$$\left|\overline{M}\left(\gamma g\rightarrow q\overline{q}\right)\right|^2 = \sum_q 16\pi^2\epsilon_q^2\alpha\alpha_s\left(\frac{\hat{u}}{\hat{t}}+\frac{\hat{t}}{\hat{u}}\right)$$

$$\left|\overline{M}\left(\gamma q\rightarrow qg\right)\right|^2 = 32\pi^2\epsilon_q^2\alpha\alpha_s\frac{4}{3}\left(-\frac{\hat{t}}{\hat{s}}-\frac{\hat{s}}{\hat{t}}\right)$$

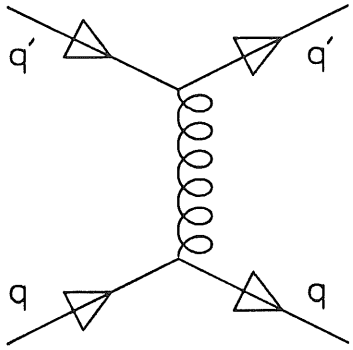

Figure A.1: $qq\prime \rightarrow qq\prime$

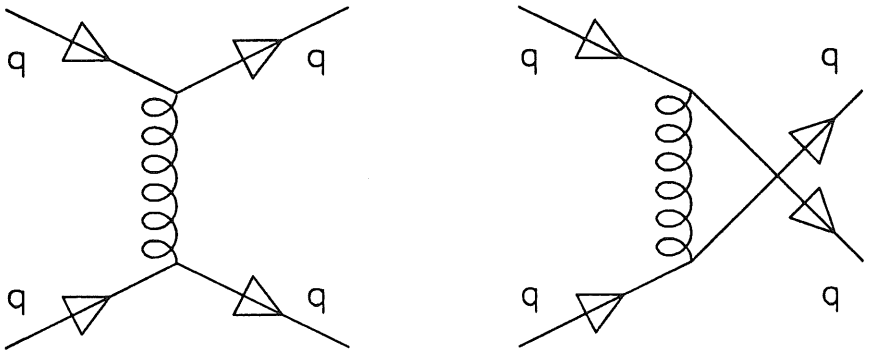

Figure A.2: $qq \rightarrow qq$

$$\frac{d\hat{\sigma}}{d\hat{t}} = \frac{\left|\overline{M}\right|^2}{16\pi\,\hat{s}^2}$$

$$\frac{d\hat{\sigma}}{d\,{p_T}^2} = \frac{\hat{s}}{\hat{s}\ + 2\hat{t}} \cdot \frac{d\hat{\sigma}}{d\hat{t}}$$

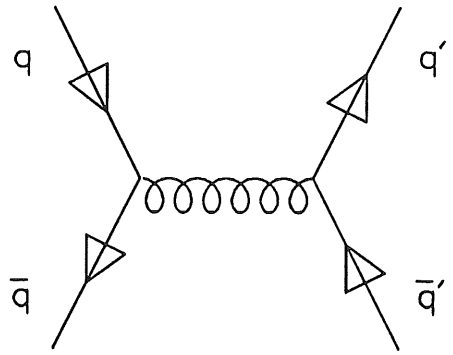

Figure A.3: $q\bar{q}\prime \rightarrow q\bar{q}\prime$

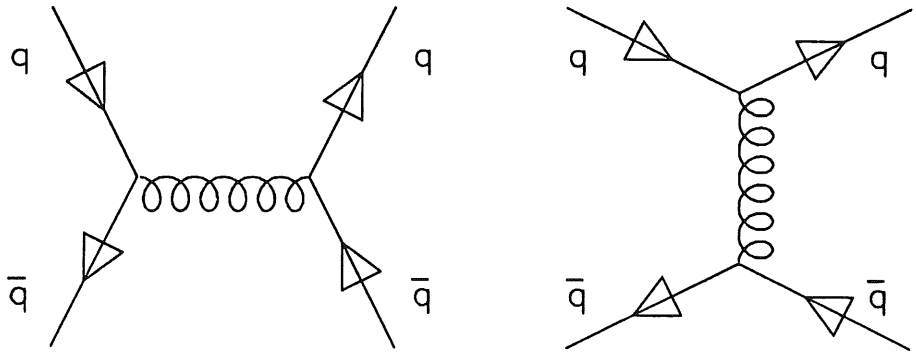

Figure A.4: $q\bar{q} \rightarrow q\bar{q}$

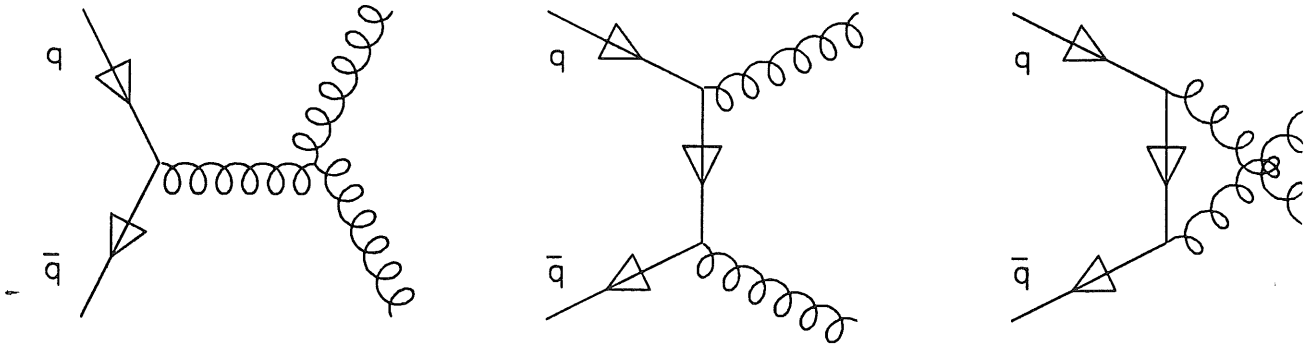

Figure A.5: $q\bar{q} \rightarrow gg$

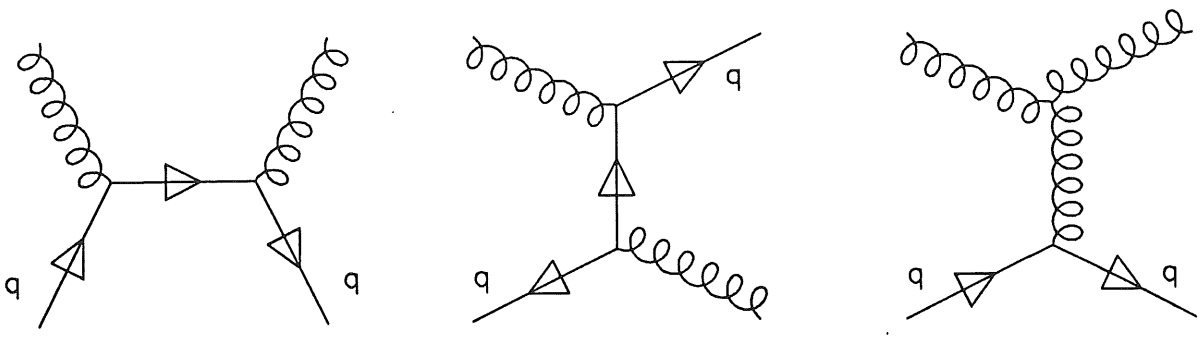

Figure A.6: $qg \to qg$

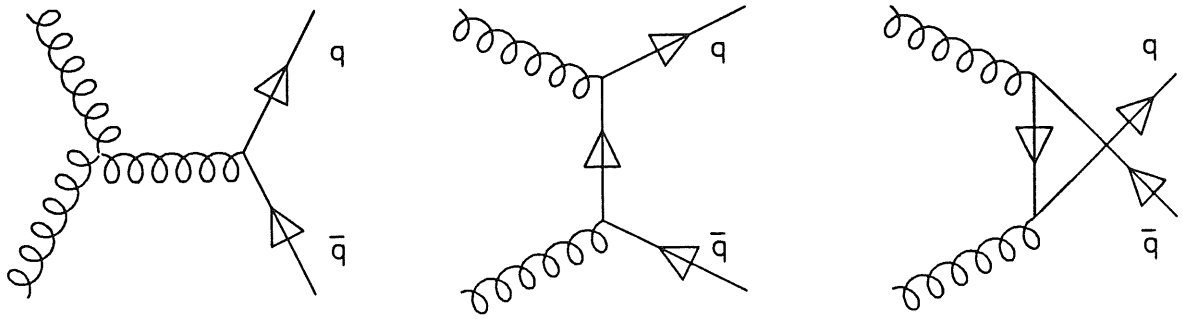

Figure A.7: $gg \to q\overline{q}$

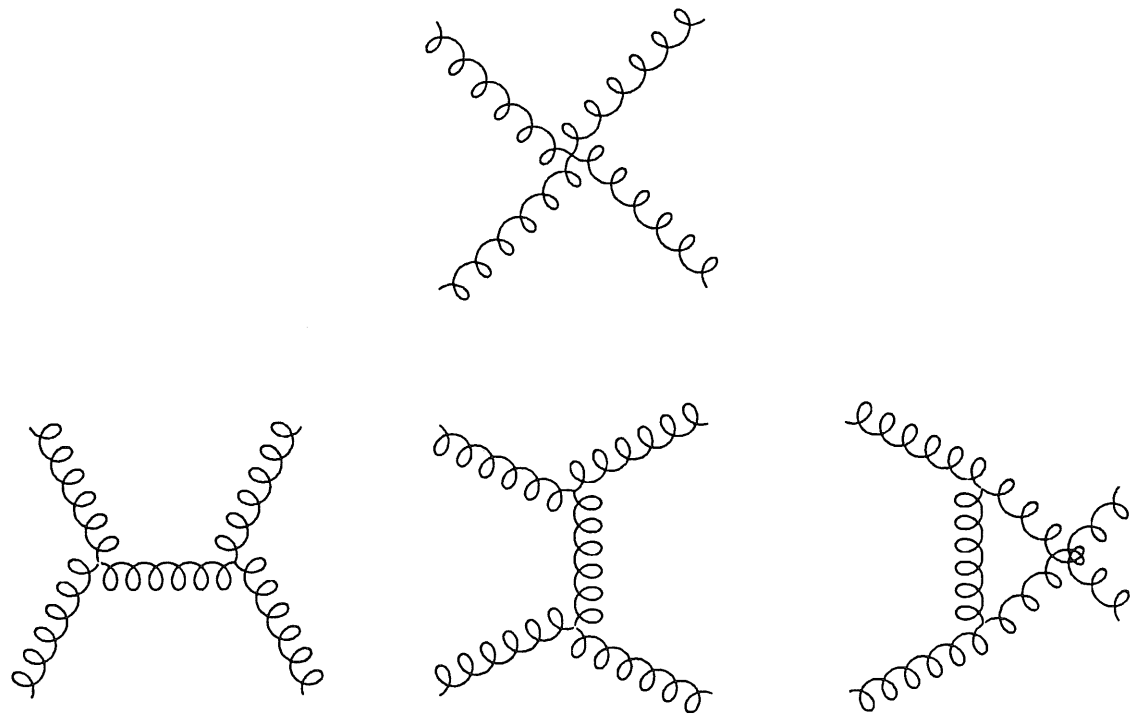

Figure A.8: $gg \to gg$

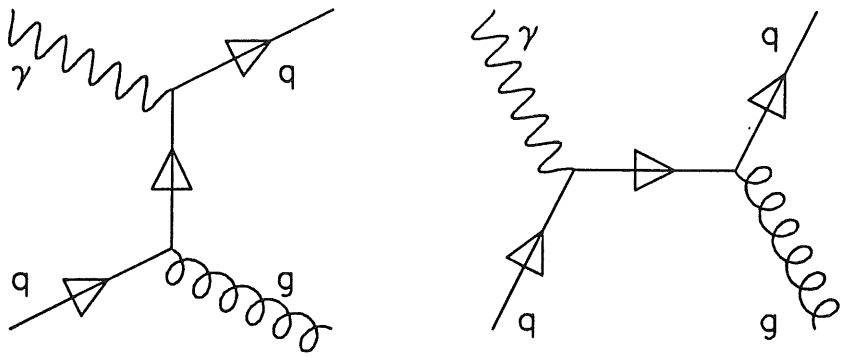

Figure A.9: QCD Compton Scattering

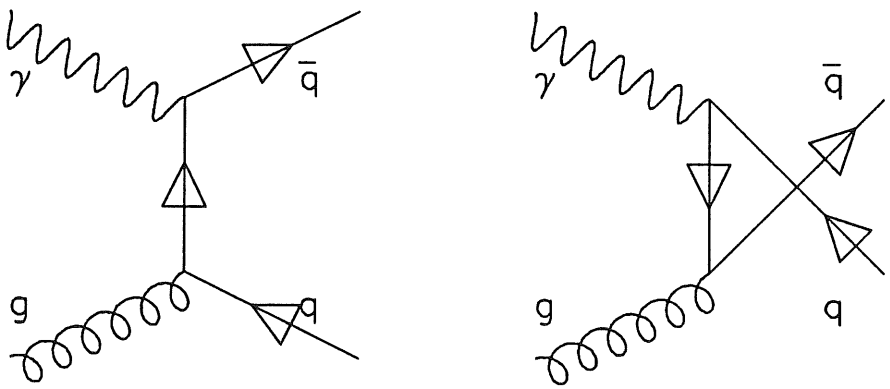

Figure A.10: Photon-Gluon Fusion

Appendix B

Structure Functions

In the following figures I have plotted the structure functions used in this study [15, 6] for a Q^2 value of 5GeV^2. In the proton the up and down valence quarks have concentrations at high x values which are not seen in the remaining 'sea' quarks. In the photon there are no valence quarks so all quarks have the same distribution as their antiquarks.

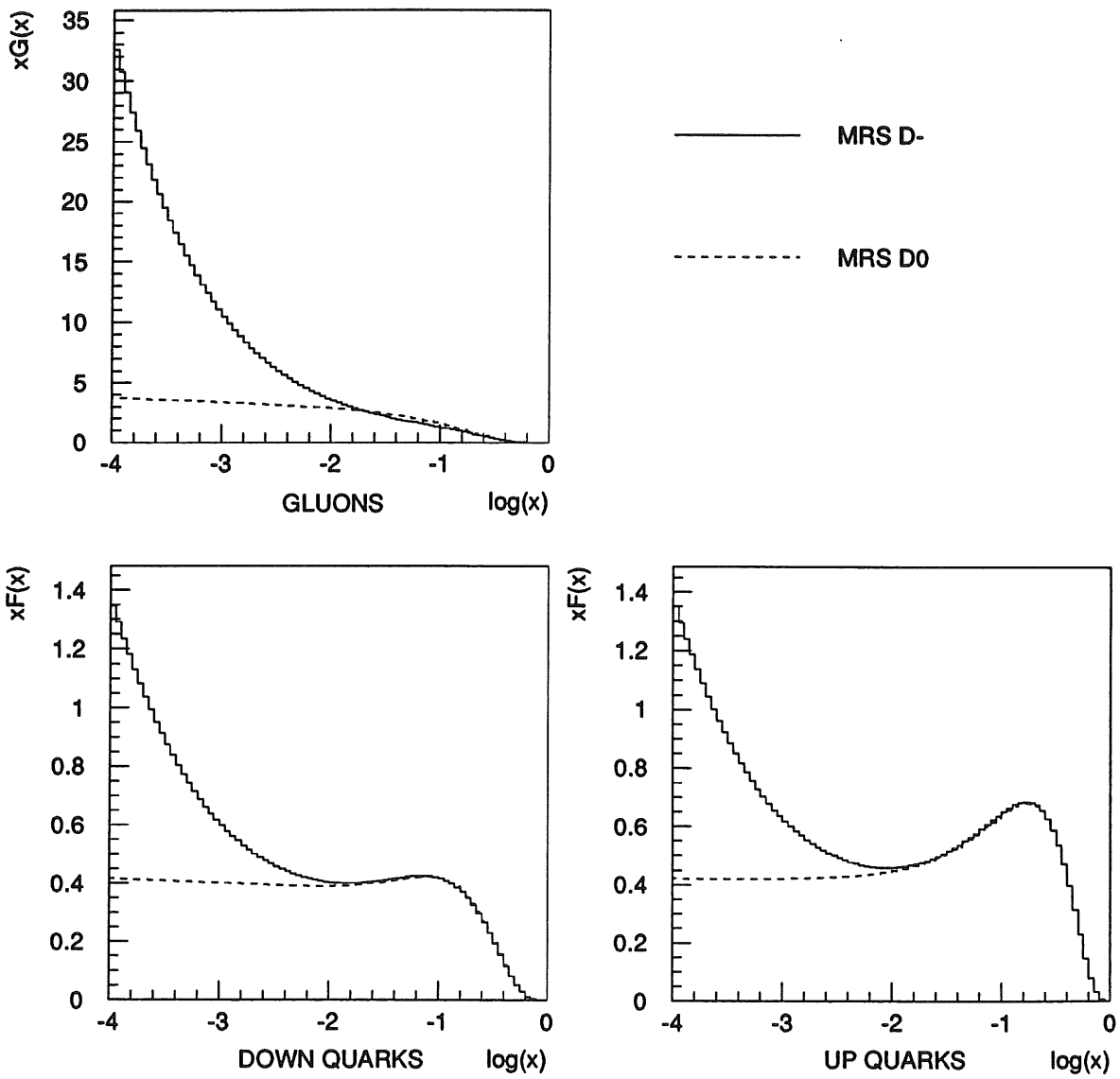

Figure B.1: Proton Structure Functions

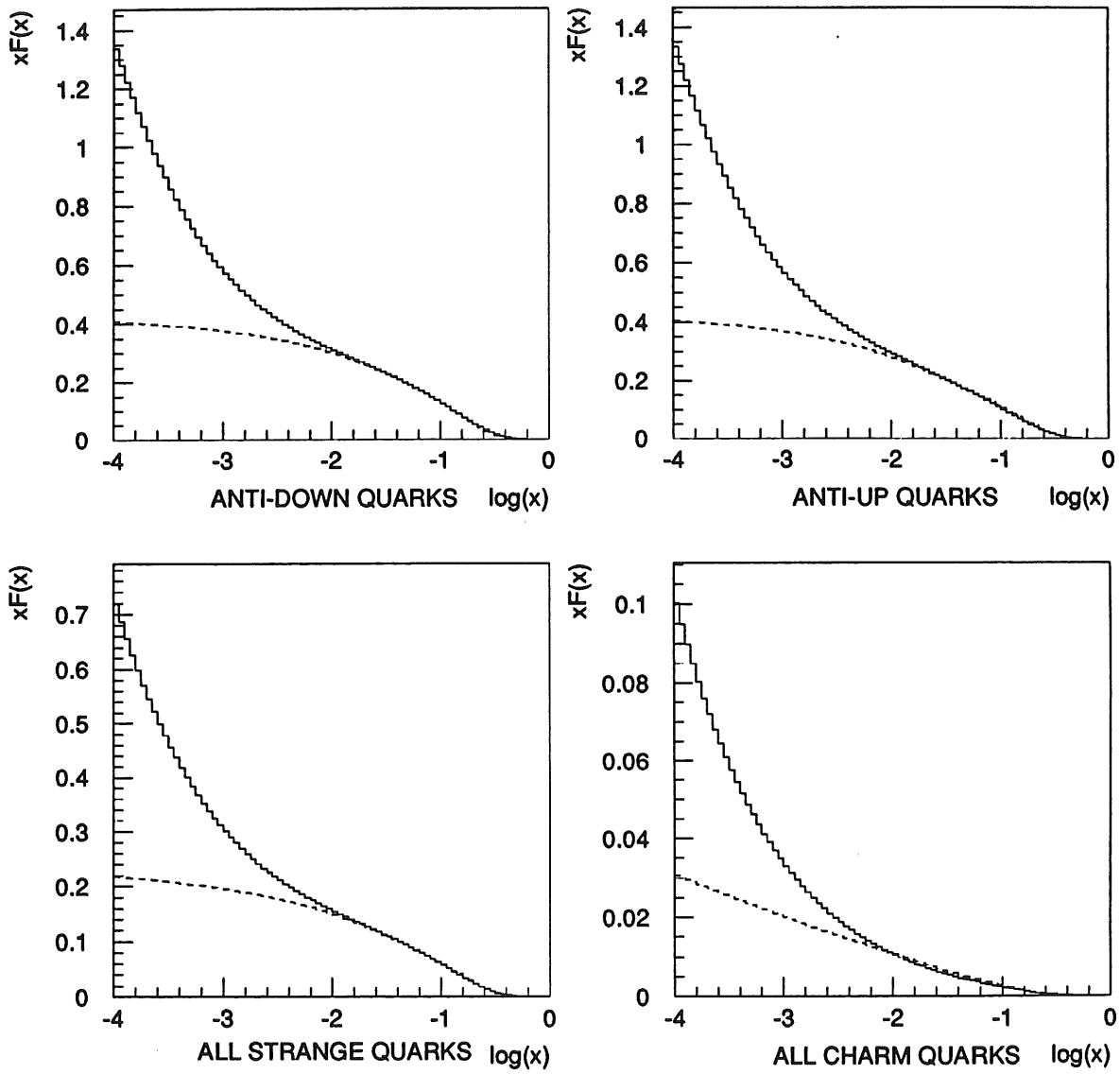

Figure B.2: Proton Structure Functions

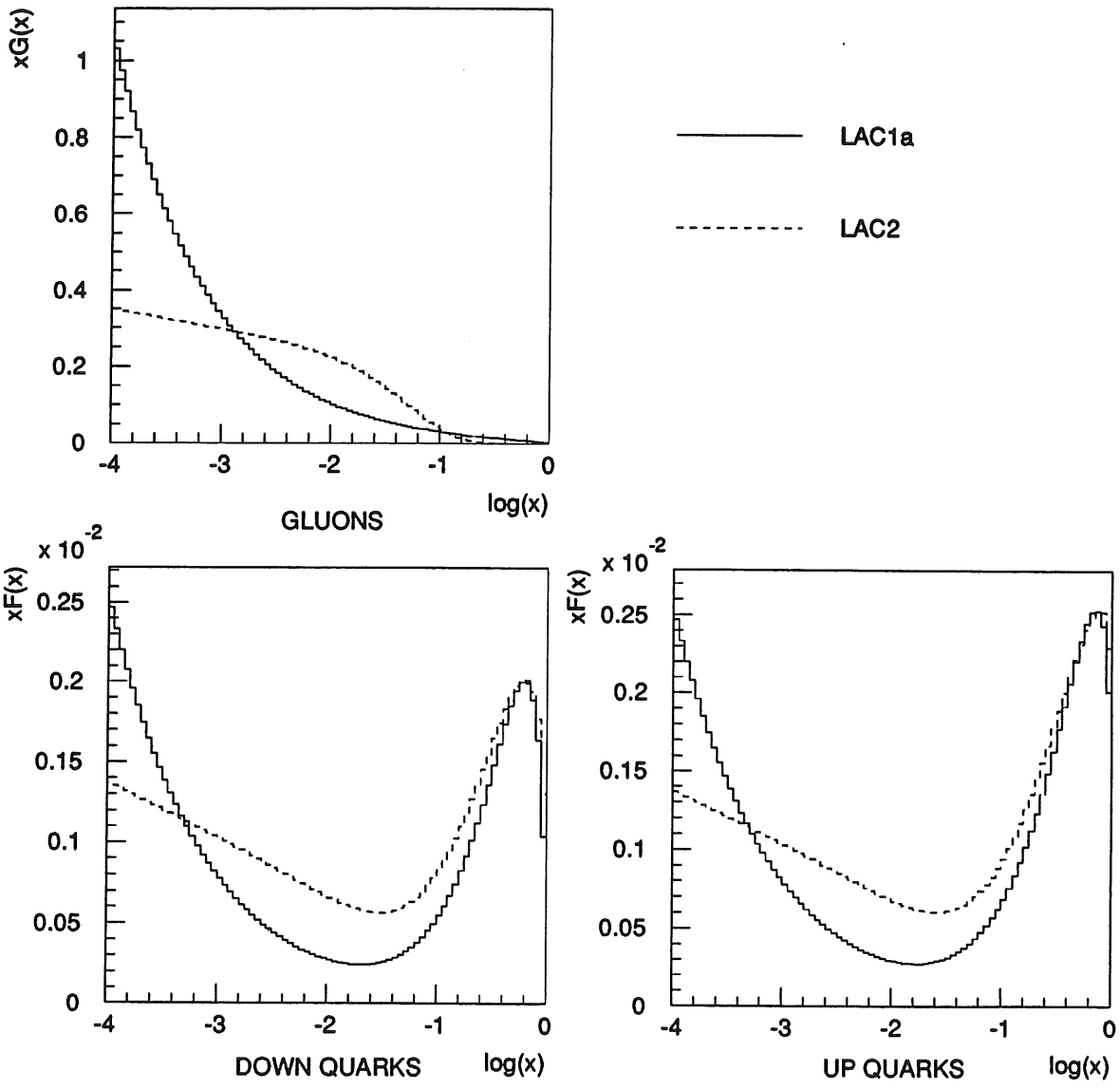

Figure B.3: Photon Structure Functions

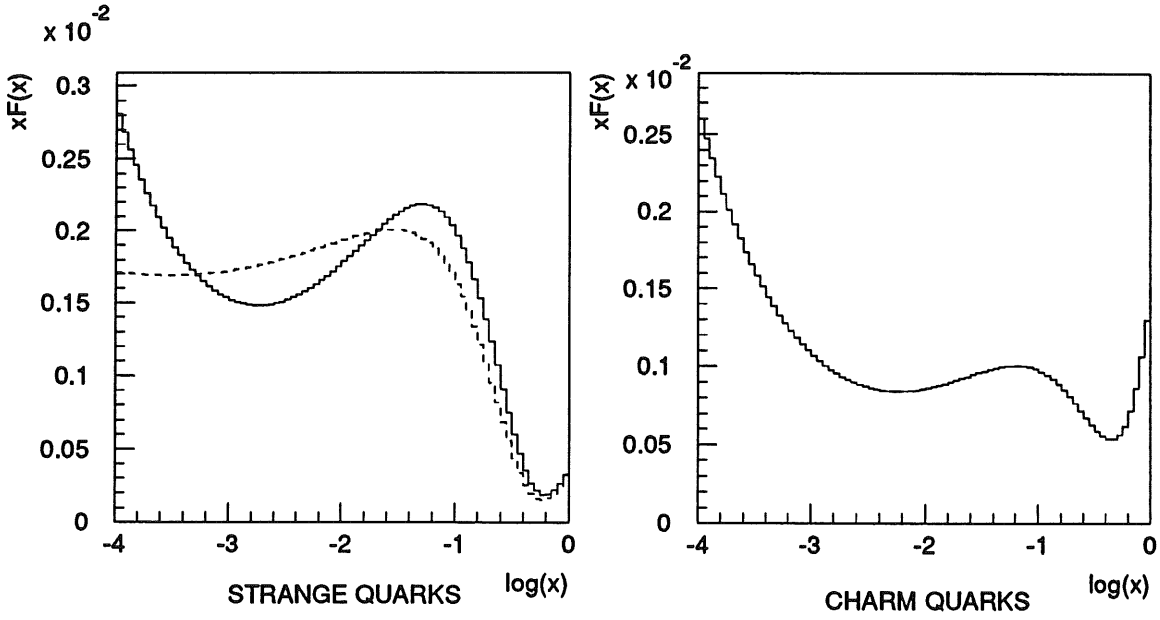

Figure B.4: Photon Structure Functions

Bibliography

[1] 'Gauge Theories in Particle Physics', I.J.R. Aitcheson and A.J.G. Hey, I.O.P. Publishing Limited, Second Edition, 1989; 'Quarks and Leptons : an Introductory Course in Modern Particle Physics', F. Halzen and A.D. Martin, John Wiley and Sons, 1984; 'Introduction to High Energy Physics', D.H. Perkins, Addison Wesley Publishing Co. Inc., Third Edition, 1987.

[2] 'Asymptotic Freedom in Parton Language', G.Altarelli and G.Parisi, Nucl.Phys.B126 (1977) p.298.

[3] 'QCD at low x: Summary', J.Bartels and J.Feltesse, in: 'Physics at HERA: Proceedings of the Hera Workshop', eds. W.Buchmueller and G. Ingelman.

[4] 'Photoproduction of Multi-Jet Events at Hera: A Monte Carlo Simulation', J.M.Butterworth and J.R.Forshaw, DESY 93-107(1993).

[5] 'Towards a Complete Description of High-Energy Photoproduction', G.A.Schuler and T.Sjoestrand, CERN-TH.6796(1993).

[6] 'Structure Function Analysis and ψ, Jet, W and Z Production: Determining the Gluon Distribution', A.D.Martin,R.G.Roberts and W.J.Stirling, Physical Review D 37(1988) p.1161-1173.

[7] 'High-p_t Hadron Production and Evidence for Hard Scattering and Measurements of Photon Structure Function F_2 at large Q^2', AMY Collaboration, in: Procn. of the IX. Intern. Workshop on Photon-Photon Collisions, eds. D.O.Caldwell and H.P.Paar (1992) p.87.

[8] 'Results From Topaz on Two Photon Hadroproduction', TOPAZ Collaboration, in: Procn. of the IX. Intern. Workshop on Photon-Photon Collisions, eds. D.O.Caldwell and H.P.Paar (1992) p.100.

[9] 'An Experimental Study of $\gamma\gamma \rightarrow$ Hadrons at LEP' ALEPH Collaboration, Phys.Lett.B 313(1993) 509-519.

[10] 'Total Photoproduction Cross Section Measurement at HERA Energies', H1 Collaboration, Physics Letters B 299(1993) 374-384.

[11] 'A Measurement of $\sigma_{tot}(\gamma P)$ at $\sqrt{s}$ = 210 GeV', ZEUS Collaboration, Phys.Lett.B293 (1992) p.465.

[12] 'The $\gamma\gamma$ Total Cross Section and the Photon Structure Functions', G.Alexander, Procn. VII. Intern. Workshop on Photon Photon Collisions, eds. A.Courau and P.Kessler (1986) p.142. 'The Structure Functions and Total Cross Sections', J.H.Field, Procn. VIII. Intern. Workshop on Photon Photon Collisions, ed. U.Karshon (1988) p.349.

[13] 'The Hadronic Properties of the Photon in High-Energy Interactions', T.H.Bauer, R.D.Spital, D.R.Yennie and F.M.Pipkin, Rev.Mod.Phys, Vol.50, No. 2, April 1978.

[14] 'Anomalous Cross Section For Photon Photon Scattering in Gauge Theories', E.Witten, Nucl.Phys.B120 (1977) p.189.

[15] 'Parametrization of Parton Distributions in the Photon', H.Abramowicz, K.Charchula and A.Levy, Physics Letters B 269(1991) p.458-464.

[16] 'A Model For Initial State Parton Showers', T.Sjoestrand, Phy.Lett.B 157(1985) 321. 'Initial State Radiation Effects on W and Jet Production', M.Bengtsson, T.Sjoestrand and M.van Zijl, Z.Phys.C 32(1986) 67.

[17] 'Coherent Parton Showers Versus Matrix Elements', M.Bengtsson and T.Sjoestrand, Phy.Lett.B 185(1987) 435. 'A Comparitive Study of Coherent and Non-Coherent Parton Shower Evolution', M.Bengtsson and T.Sjoestrand, Nucl.Phys.B 289(1987) 810.

[18] 'Parton Fragmentation and String Dynamics', B.Andersson, G.Gustafson, G.Ingelman and T.Sjoestrand, Phys.Rep.97(1983) 31. 'Jet Fragmentation of Multiparton Configurations in a String Framework', T.Sjoestrand, Nucl.Phys.B 248(1984) 469.

[19] 'Corrections to Weizsacker-Williams approximation for low-Q^2 inelastic ep scattering', A.Lebedev, in: Proc. Workshop on Physics at HERA, DESY, Hamburg, FRG, 1992) p.613.

[20] 'PYTHIA 5.6 and JETSET 7.3 Physics and Manual', Torbjörn Sjöstrand, CERN-TH.6488/92.

[21] 'The e-p Collider HERA', D.Degele, Report at the 3rd European Particle Accelerator Conference in Berlin, DESY 92-12 (1992).

[22] 'The H1 Technical Report', H1-Collab, to be published in Nuclear Instrumentation and Methods.

[23] 'The Magnetic Field Mapping of the H1 Magnet', D.Newton, H1-08/90-143.

[24] 'Fine Structure Effects in the H1 Magnetic Field', D.Newton, H1-08/90-143.

[25] 'The Central Jet Chamber of the H1-Detector at HERA', J.Buerger et al., H1-TR 200.

[26] 'Z-Kalibration und dE/dx-Kalibration der Zentralen Spurenkammer des H1-Detektors', S.Prell, Internal Report DESY FH1T-92-04.

[27] 'The Fast H1 Detector Monte Carlo', Michael Kuhlen, Talk at the XXVI International Conference on H.E.P., Dallas 1992.

[28] 'Photoproduction at HERA: A summary of the discussions of the working group on photoproduction', J.K.Storrow, in the proceedings of the workshop 'HERA - the new frontier of QCD' held in Durham, England, March 22-26 1993. J.Phys.G Vol.19 Number 10(1993) 1641-1657.

[29] 'Measurement of the Hadronic Final State in Deep Inelastic Scattering at HERA', H1 Collaboration, Physics Letters B 298(1993) 469-478.

[30] 'RAYPHOTON 2.0: An interface for HERA photoproduction physics', N.H.Brook, A.DeRoeck and A.T.Doyle, in: 'Physics at HERA: Proceedings of the Hera Workshop', eds. W.Buchmueller and G. Ingelman.

[31] 'LUCIFER - A Monte Carlo for High P_t Photoproduction', G.Ingelman and A.Weigend, Computer Physics Communications 46(1987) 241.

[32] 'New Results from the H1 Experiment at HERA on Photoproduction, Deep Inelastic Scattering and Searches for New Particles', H1 Collaboration, DESY 93-077 (June 1993).

[33] 'Hard Scattering in photon-proton Interactions', H1 Collaboration, Physics Letters B 297(1992) 205-213.

[34] 'Quantum Chromodynamic Gluon Contributions to Large-P_T Reactions', R.Cutler and D.Sivers, Phys.Rev.D17 Vol.1(1978) 196.